

# Mapping the seismic noise field in Europe: spatio-temporal variations in wavefield composition and noise source contributions

Yang Lu<sup>1,2</sup>, Helle A. Pedersen<sup>1</sup>, Laurent Stehly<sup>1</sup> and AlpArray Working Group

<sup>1</sup>CNRS, Université Grenoble Alpes, Université Savoie Mont Blanc, IRD, Université Gustave Eiffel, ISTerre, 38000 Grenoble, France. E-mail: [Helle.Pedersen@univ-grenoble-alpes.fr](mailto:Helle.Pedersen@univ-grenoble-alpes.fr)

<sup>2</sup>Department of Earth Sciences and Southern California Earthquake Center, University of Southern California, Los Angeles, CA, USA

Accepted 2021 July 8. Received 2021 June 3; in original form 2020 December 14

## SUMMARY

We study spatial and temporal characteristics of the microseismic noise field across Europe. Rather than focusing on the areas of noise generation, the scope of this work is to characterize, at the scale of Europe, the spatio-temporal evolution of the noise wavefield that results from the interplay of the seismic noise sources and the propagation effect. To that end, we perform single station analysis in three period bands (PB1: 2.5–5 s; PB2: 5–10 s and PB3: 10–20 s) using three-component seismic data recorded by ~1000 broad-band stations in the time period 2011–2019. We calculate, for each period band, station and day, a set of parameters that are practically possible to apply to a large data set, yet yields insight into the spatio-temporal evolution of the wavefield. These parameters are: the total energy level, the dominant period of the Primary and Secondary microseismic peaks, the horizontal direction with the most energy, the horizontal direction of the dominant Rayleigh waves and the square root of the energy ratio between the horizontal and vertical components. The analysis of these parameters shows that the noise field in Europe is dominated by surface waves from the North Atlantic Ocean with, in PB1 and PB2, an additional and significant contribution from the eastern part of the Mediterranean Sea. The relative contribution of these two source regions depends on the season, the influence of the eastern Mediterranean Sea being strongest in summer. The map of the peak period of the Primary and Secondary microseismic peaks indicates that the relative contribution of these two source regions is frequency dependent: the period of the Primary microseismic peak exhibits an overall increase with distance to the North Atlantic Sources, because of stronger attenuation of high-frequency wave contents. By contrast, the period of the Secondary microseismic peak is simultaneously influenced by sources in both the North Atlantic Ocean and eastern Mediterranean Sea. We show that in both microseismic peaks (PB2 and PB3), the wavefield is dominated by Love waves, as the horizontal components have the highest energy at approximately 90° angle to the direction of elliptical polarization. Moreover, our results show that lateral heterogeneities in the crust have a major influence on the noise field. In particular, the propagation directions of Love and Rayleigh waves show strong dependency on location (but not on time of year), with very sharp boundaries for example at the edge of the Alps. Thus, the scattering that takes place in the heterogeneous Alpine crust partly randomizes the directions of the microseismic wavefield in particular in PB1 and PB2. Finally, we show that the temporal evolution of the amplitude ratio between the horizontal and vertical components reflects the relative amounts of surface waves from the North Atlantic Ocean with respect to body waves from sources in the Southern Hemisphere. Thus, this ratio can be used as a proxy to identify time periods where body waves are significant in the noise wavefield.

**Key words:** Seismic instruments; Seismic interferometry; Seismic noise.

## 1 INTRODUCTION

Seismic noise has been of interest to seismologists since the middle of the 19th century (see review by Milne 1886). The link between microseismic signals and weather systems in the North Atlantic Ocean was firmly established already in the beginning of the 20th century (e.g. Klotz 1908; Gutenberg 1912). Gutenberg in particular compared observations of the Secondary microseismic peak in Europe and Canada and linked them to weather systems in the North Atlantic Ocean (Gutenberg 1921, 1931). Since the seminal work of Longuet-Higgins (1950), the source of seismic noise in the Secondary microseismic peak ( $\sim 3$  to  $\sim 10$  s period) is understood to be created by interacting waves and associated pressure variations at the seafloor. The noise in the Primary microseismic peak can be explained by single wave interaction with seafloor topography (Hasselmann 1963). For both mechanisms, further complexity occurs due to variations of seafloor bathymetry and lateral heterogeneity, leading to wave diffraction and scattering around the source area and along the propagation path (e.g. Cessaro 1994; Fukao *et al.* 2010; Saito 2010; Arduin 2018).

Since it was demonstrated that seismic noise can be used for imaging (Shapiro & Campillo 2004; Sabra *et al.* 2005; Shapiro *et al.* 2005) and monitoring (Brennguier *et al.* 2008) of the Earth's interior, the interest in seismic noise continues to increase. A difficulty in such studies resides in the inhomogeneous source distribution which can result in spurious phases in the noise correlations, or bias the observed velocities (Snieder *et al.* 2006; Pedersen *et al.* 2007; Ruigrok *et al.* 2008; Fan & Snieder 2009; Froment *et al.* 2010; Snieder & Sens-Schönfelder 2015; Poli *et al.* 2017; Pedersen & Colombi 2018). Some of these spurious arrivals are related to earthquakes (e.g. Boué *et al.* 2014; Poli *et al.* 2017; Li *et al.* 2020); noise correlations at global scale shows arrivals created by cross terms of seismic waves and modes from earthquakes, because these signals are coherent over large geographic scales.

The noise coda is less sensitive to the anisotropy of the noise field than the direct wave (Colombi *et al.* 2014). Even so, seismic velocities, as observed from analysis of the noise coda, show yearly variations which must be corrected for prior to interpreting velocity variations in terms of tectonic activity (Brennguier *et al.* 2008, 2012) or environmental forcing (Meier *et al.* 2010; Lecocq *et al.* 2017). Other applications of seismic noise, such as the calculation of H/V ratios to constrain Earth structure, may be hindered by seasonal changes (e.g. Tanimoto *et al.* 2006).

The main locations worldwide of noise sources of *P* waves in the Secondary microseismic peak are well known (e.g. Gerstoft *et al.* 2008; Landes *et al.* 2010). As numerous studies show, the situation for surface waves is more complex, probably due to upper crustal heterogeneity and bathymetry. Overall, the seismic noise in the Primary and Secondary microseismic peaks remains dominated by fundamental mode Love and Rayleigh waves, as well as sub-vertically propagating *P* waves. The inferred source areas may not coincide for the different wave types, even within a given frequency range (e.g. Gal *et al.* 2017), and other wave types may also be present (e.g. Kimman *et al.* 2012; Liu *et al.* 2016; Nishida & Takagi 2016). Note that the noise sources both at lower ( $< \sim 0.05$  Hz) and higher ( $> \sim 0.5$  Hz) frequencies are different to those producing the Primary and Secondary microseismic peaks (e.g. Nishida *et al.* 2008; Koper *et al.* 2010); these frequency ranges are not addressed here.

The further development of noise-based methods for imaging and monitoring can be supported through a better understanding of the composition of the noise field, and its variation over time and space.

While small-scale seismic arrays are well adapted for separating different wave types (e.g. Haubrich & McCamy 1969), only few such arrays are available so the spatially continuous characterization of the wavefield is generally not possible with array-based methods. Another end-member, of which only a few studies are available, is to characterize the noise field over large areas using single station measurements (Koper & Burlacu 2015; Takagi *et al.* 2018).

Many studies have been dedicated to characterizing the sources of seismic noise in Europe, using for example distant arrays within Europe (Essen *et al.* 2003; Chevrot *et al.* 2007; Juretzek & Hadziioannou 2016), arrays or seismic stations on different continents (e.g. Friedrich *et al.* 1998; Stehly *et al.* 2006; Kedar *et al.* 2008; Sergeant *et al.* 2013; Retaillieu *et al.* 2017), or permanent and temporary arrays in many different locations (e.g. Pedersen *et al.* 2007; Moni *et al.* 2013; Beucler *et al.* 2014; Tanimoto *et al.* 2015; Craig *et al.* 2016; Lepore & Grad 2018), including using ring laser equipment (Tanimoto *et al.* 2016). All these studies point towards the North Atlantic Ocean (south of Greenland, west of Ireland) as the major source area for surface waves, with some variety about the additional locations of the noise sources, depending on frequency band, arrays used, and period (month/year) under analysis. Local noise sources from the Mediterranean Sea are also identified using stations close to the Mediterranean coast. These stations have a relatively high frequency Secondary microseismic peak: above 0.2 Hz, and possibly nearer 0.25 Hz (Marzorati & Bindi 2006; Marzorati & Bindi 2008; Evangelidis & Melis 2012; Ferretti *et al.* 2013).

In terms of lateral variations of seismic noise at European scale, the study by Juretzek & Hadziioannou (2016) may be the most complete today, combining array analysis from eight different locations with a special focus on the relative strength of Rayleigh and Love waves, the source directions from the two types of waves, and the differences between summer and winter. They show that the relative energy of the two wave types does, in Europe, not depend on the season. When Love waves are present, Rayleigh waves from the same direction are present, while the opposite is not always the case. Generally, the Love waves have higher kinetic energy than Rayleigh waves for the Primary microseismic peak, and significant variations with azimuth. On the contrary, Rayleigh to Love wave kinetic energy ratios are independent of azimuth in the Secondary microseismic band, and is, with a few exceptions, smaller than one. Based on combined analysis of broad-band and ring laser data, Tanimoto *et al.* (2015, 2016) studied Rayleigh to Love wave energy ratios at Zettzell, Germany. They also concluded on higher Love wave energy than Rayleigh wave energy during most of the year, but with a change to higher Rayleigh than Love wave energy during the summer months.

This study aims at describing the noise field and its temporal variations across Europe. The scope is twofold. First, such results can shed light on the relative strength of different noise sources that affect the noise field across Europe during the year. Second, we wish to better understand the noise wavefield in Europe, and its spatial and temporal evolutions, which are due to the relative strength of different source areas and to propagation effects, in particular frequency dependent and spatially varying scattering and attenuation. The understanding of the noise field is paramount to build the next generation approaches on how to analyse seismic noise, to ensure fast conversion of the Green's function for specific waves, for creating analysis methods based on specific noise areas, and to understand potential bias in the retrieved noise correlations. We use single station observations, supported with array analysis from a central location within the study area. To carry out this analysis we take advantage of the present high density of seismic

stations, due to an increasing number of permanent stations, and large temporary seismic deployments such as AlpArray (AlpArray Seismic Network 2015). While this study is organized in a way that highlights our choice of main outcomes, we believe that further information can be found in our observations. Consequently, we present the observations in a format and with a completeness aimed also at future use.

## 2 DATA AND DATA PROCESSING

We analysed seismic broad-band stations (three components) within latitudes 30°N–65°N and longitudes 10°W–30°E, for one decade of data (2011–2019), and for which data are distributed by the ORFEUS service European Integrated Data Archive, EIDA (Strollo *et al.* 2021). We also included a presently embargoed data set, AlpArray (AlpArray seismic network 2015). All seismic networks are listed in Section 5 (Data Availability). We used only stations in N-E-Z orientation, because the number of other orientations was negligible.

Each daily record was detrended, filtered between 0.004 and 0.4 Hz, decimated to 1 Hz sampling rate and corrected for the instrument response (converted into velocity in  $\text{m s}^{-1}$ ). Furthermore, we performed an initial quality control to remove daily records that contain more than 18 gaps or less than 64 800 s (18 h) of data.

In total, 3 component data from 1480 stations from 73 seismic networks were used for further analysis, representing 1.4 Tbytes of data after downsampling to 1 Hz. The initial data set volume analysed is at least 100 times that volume, that is, > 140 Tbytes, taking into account initial sampling rate and data rejection. Permanent networks, combined with the AlpArray temporary network and past temporary deployments, provide a dense station coverage in the Alpine and Apennine regions with interstation distance  $\sim 50$  km. The station coverage in the rest of the study region is variable.

During the course of the data analysis, we applied further quality criteria. Common to all data analysis is that we excluded daily files for which not all three components were available, and stations for which there were not at least 6 months of data, with at least one month of data between May and September, and one month of data between November and March. Approximately 35 per cent of the initial station list was rejected, a number which should be seen in the light of the number of temporary experiments, including those of short duration, which were present in the initial station list. Fig. 1 shows the location of the 978 seismic stations remaining after this further quality control, with the colour code indicating the available number of days of this pre-processed data set. Fig. 1 also shows the main tectonic units across the study area.

Data analysis was carried out for 20-min segments, that is, with up to 72 segments per day. Except for the calculation of the dominant period peaks, all analyses were carried out after filtering in three period bands, corresponding to periods PB1: 2.5–5 s, PB2: 5–10 s and PB3: 10–20 s. These period bands are standard to separate the Primary and Secondary microseismic peaks (10 s period as the limit between PB2 and PB3), to capture the peak of the Secondary microseismic peak at  $\sim 7$  s period (PB2 centred around that period) and to capture the high-frequency end of the Secondary microseismic peak. To exclude outliers due to for example earthquakes, glitches and other instrument problems, we defined the daily measurement of any given parameter by the median value over all the 20-min windows within the day. The efficiency of this procedure was checked on a subset of the data. The only exception was  $\theta_E$  and  $\theta_R$ , for which

we calculated the mean unit vector using the angle for each time window.

Many observations can be carried out on single station data, but the use of only three components implies that different retrieved parameters are linked. We here focus on observations that are simple, therefore optimal in terms of computation on this very large data set, yet illustrate the insights that we acquired during the data analysis. In addition, the chosen parameters have a certain level of independency, related to the independency between the overall amplitude level, the amplitude ratio between components, the phase difference between components in the three target period bands and the shape of the amplitude spectrum. The retrieved parameters are:

(i)  $E$ : the sum of squared amplitudes  $E_N$ ,  $E_E$  and  $E_Z$  over the recordings of the three components ( $u_E$ ,  $u_N$ ,  $u_Z$ ) in the time domain, divided by window length.

(ii)  $T_P$ : dominant period of the Primary microseismic peak: the period corresponding to the local maximum of the spectral amplitude within the period interval 10–20 s (PB3). We therefore assume that the Primary microseismic peak lie within that interval (see Sections 3 and 4). We checked that we obtain the same values for  $T_P$  independently of the component, so in the figures we only show  $T_P$  as observed on the vertical component. If there is a single source area and assuming that the quality factor varies very little at periods close to  $T_P$ ,  $T_P$  should overall increase with distance to the source, due to higher attenuation over space at shorter periods.

(iii)  $T_S$ : dominant period of the Secondary microseismic peak: as the Secondary microseismic peak dominates the spectrum,  $T_S$  can be estimated as the period of the maximum spectral amplitude within the period interval 2.5–10 s. As for  $T_P$  we only show the value of  $T_S$  observed on the vertical component. If there is a single source area and assuming that the quality factor varies very little at periods close to  $T_S$ ,  $T_S$  should overall increase with distance to the source.

(iv)  $T_P/T_S$ : ratio of dominant period of Primary and Secondary peaks. Note that we take the ratio of daily  $T_P$  and  $T_S$  values, then average over either the year (all available time windows), summer and winter months. If the Primary and Secondary microseismic peaks have their origin in the same source area, this ratio should be 2 (Longuet-Higgins 1950) close to the source, and evolve slowly with distance because the spectrum will change shape due to wave attenuation. Spatial variations of  $T_P/T_S$  can therefore be indicative of the presence of a single or several source areas.

(v)  $\theta_E$ : azimuth of the horizontal direction in which the summed squared amplitudes is maximum. This analysis follows the method by Flinn (1965): the signal eigenvalues ( $\lambda_1$ ,  $\lambda_2$ ,  $\lambda_3$ ), sorted so  $\lambda_1 > \lambda_2 > \lambda_3$ , are calculated as solutions to  $(\text{cov}[u_E, u_N, u_Z] - \lambda_i \mathbf{I})\mathbf{v}_i = 0$  where  $\mathbf{I}$  is the identity matrix,  $\mathbf{v}_i$  is the eigenvector associated with the eigenvalue  $\lambda_i$  and  $\text{cov}[u_E, u_N, u_Z]$  indicates the covariance matrix of the three components. In that case, the azimuth of highest energy within the time window under consideration is calculated by:

$$\theta_E = \arctan\left(\frac{v_{1,2}}{v_{1,1}}\right)$$

with the coordinates defined and periodicity applied so that  $\theta_E$  is the clockwise angle from north.

(vi)  $\theta_R$ : dominant direction of propagation of the Rayleigh waves within the signal. We here follow the general strategy of Hobiger *et al.* (2009). We rotate the horizontal components ( $u_H = u_N \cdot \sin\theta + u_E \cdot \cos\theta$ ) between 0° and 180° with steps of 1° in  $\theta$ , until we find the direction  $\theta_R$  for which the vertical component is

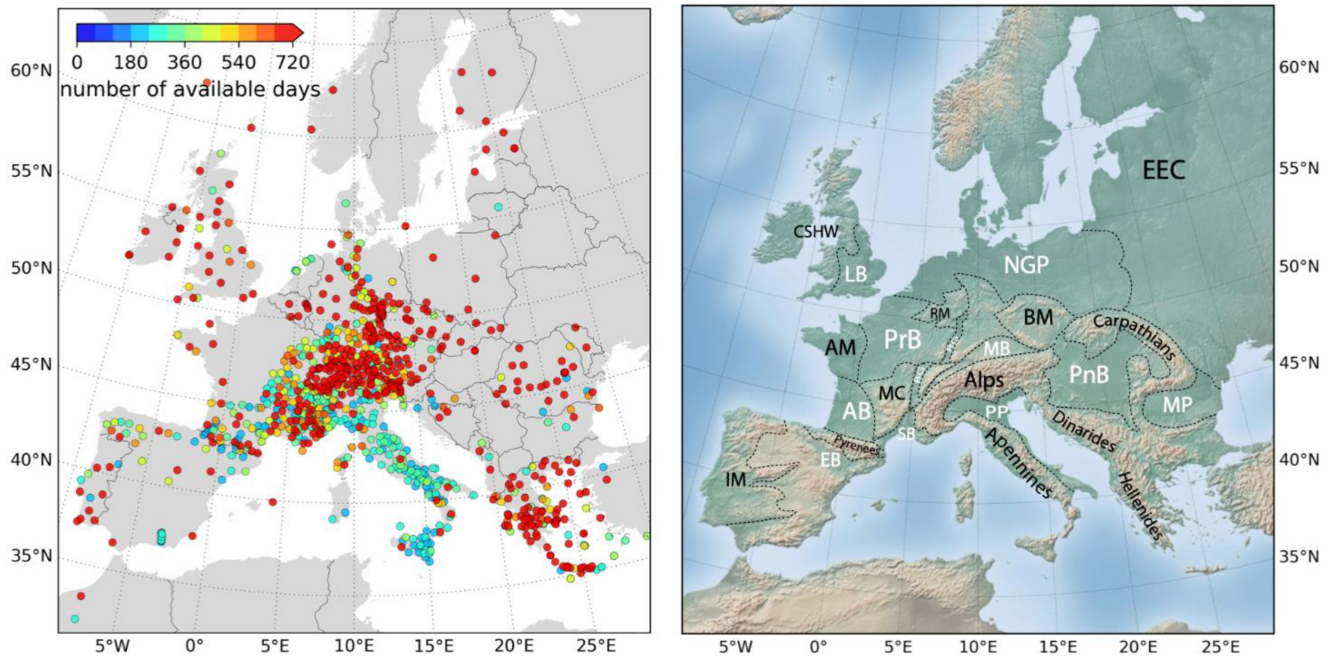


**Figure 1.** Left: map of the 978 seismic stations used in this study. The colour scale denotes number of available days with qualified daily recordings for each station. Right: main geological units in Europe (modified from Neubauer 2003t; Schmid *et al.* 2004; Handy *et al.* 2010). AB, Aquitaine Basin; AM, Armorican Massif; BG, Bresse Graben; BM, Bohemian Massif; CSHW, Central Plain, Southern Uplands, Highlands and Wales Salop of UK; EB, Ebro Basin; EEC, Eastern European Craton; IM, Iberian Massif; LB, London Basin; MB, Molasse Basin; MC, Massif Central; MP, Moesian platform; NGP, North German Plain; PnB, Pannonian Basin; PP, Po Plain; PrB, Paris Basin; RG, Rhine Graben; RM, Rhine Massif; SB, Southeast Basin of France.

the closest fit to a  $90^\circ$  phase shift with the rotated horizontal component. Once the direction with best  $90^\circ$  phase shift is found, we determine the propagation direction by assuming that the Rayleigh wave has retrograde polarization. This assumption will be correct at long periods, but may not be valid at short periods in sedimentary basins. The angle we refer to in the figures is the direction (from north) from which the waves are incoming, that is, equivalent to backazimuth at a station for earthquake data, so  $0^\circ$  corresponds to waves incoming from north,  $90^\circ$  from east,  $180^\circ$  from south. Takegi *et al.* (2018) showed such polarization analysis is stable also for distributed sources, for which the polarization analysis will show the centroid of the propagation directions of the incident Rayleigh waves. Similar values of  $\theta_E$  and  $\theta_R$  would be indicative of the dominance of Rayleigh waves, while a  $90^\circ$  difference would indicate that Love waves dominate the horizontal component.

(vii)  $A_H/A_V$ : the square root of  $(E_N + E_E)/E_Z$ . Note that to stabilize the calculation we use the daily values of  $E_N$ ,  $E_E$  and  $E_Z$  to obtain the daily values of  $A_H/A_V$ . While  $A_H/A_V$  in the period bands under study is mainly related to crustal structure, we will subsequently show that the variations of  $A_H/A_V$  over time in our case informs on the composition of the wavefield.

As our aim is to characterize the noise field that dominates over long time periods, we diminished the influence of earthquakes, exceptionally high amplitude noise activity and instrument problems (spikes, mass centre issues and instrument response issues) by excluding daily records with  $E$  larger than  $10^{-6} \text{ m}^2 \text{ s}^{-2}$  in PB1 and in PB2, and  $10^{-7} \text{ m}^2 \text{ s}^{-2}$  in PB3. We also removed daily records showing spurious  $A_H/A_V$  where: (i) the standard deviation of  $A_H/A_V$  measurements in 20-min segments is larger than 0.5; and (ii) the daily  $A_H/A_V$  differs more than 0.5 from its median value over all available days. These criteria combined led to exclusion of some of

the stations that had signal and instrument response problems and therefore appeared as outliers throughout the analysis.

Fig. 2 shows an example of analysis for a single station, FUSIO, part of the Switzerland seismic network [Swiss Seismological Service (SED) at ETH Zurich 1983], located in a central position of the study area. Seasonal variations of  $E$ , that is, higher noise levels in winter than in summer, are clear for all frequency bands. For this particular station, the seasonal variations (peak to trough) are of the same order as the difference between the Primary and Secondary microseismic peaks (peak of PB3 and peak of PB2).

The shape of the spectra means that it is inherently easier to measure  $T_S$  than  $T_P$  (peak periods), as  $T_S$  corresponds to the global maximum and  $T_P$  to a local maximum within a broad spectrum.  $T_S$  shows very clear seasonal variations, with dominance of  $T_S = 6\text{--}7$  s in winter and  $T_S = 4\text{--}5$  s in summer.  $T_P$  is more noisy, with typical summer values of 13–14 s in winter, switching to  $\sim 16$  to 17 s in summer. Note that  $T_P$  decreases from winter through spring, then jumps to longer periods in summer. This occurs at times in the year where  $T_S$  is small, so  $T_P$  could potentially decrease to values below the search interval of 10–20 s. The same phenomenon is observed at other stations across the study area, especially for stations close to the Mediterranean Sea. We verified that there is no local maximum corresponding to a short period ( $< 10$  s) value for  $T_P$ . In some locations, and in particular in Greece, there is for some stations the hint of a slight bump (a few dB) in the spectrum at periods of approximately twice that of  $T_S$ , when  $T_S$  is small. This bump would correspond to a local maximum fully absorbed within the steep spectrum of the Secondary microseismic peak (see Fig. S1 in Supporting Information). The bump would correspond to a splitting of either the Primary microseismic peak, or of the Secondary microseismic peak, as observed by, for example, Bromirski *et al.* (2005), Koper & Burlacu (2015) and Xiao *et al.* (2018). The small bump can be missed by our analysis, but is not a prevalent feature

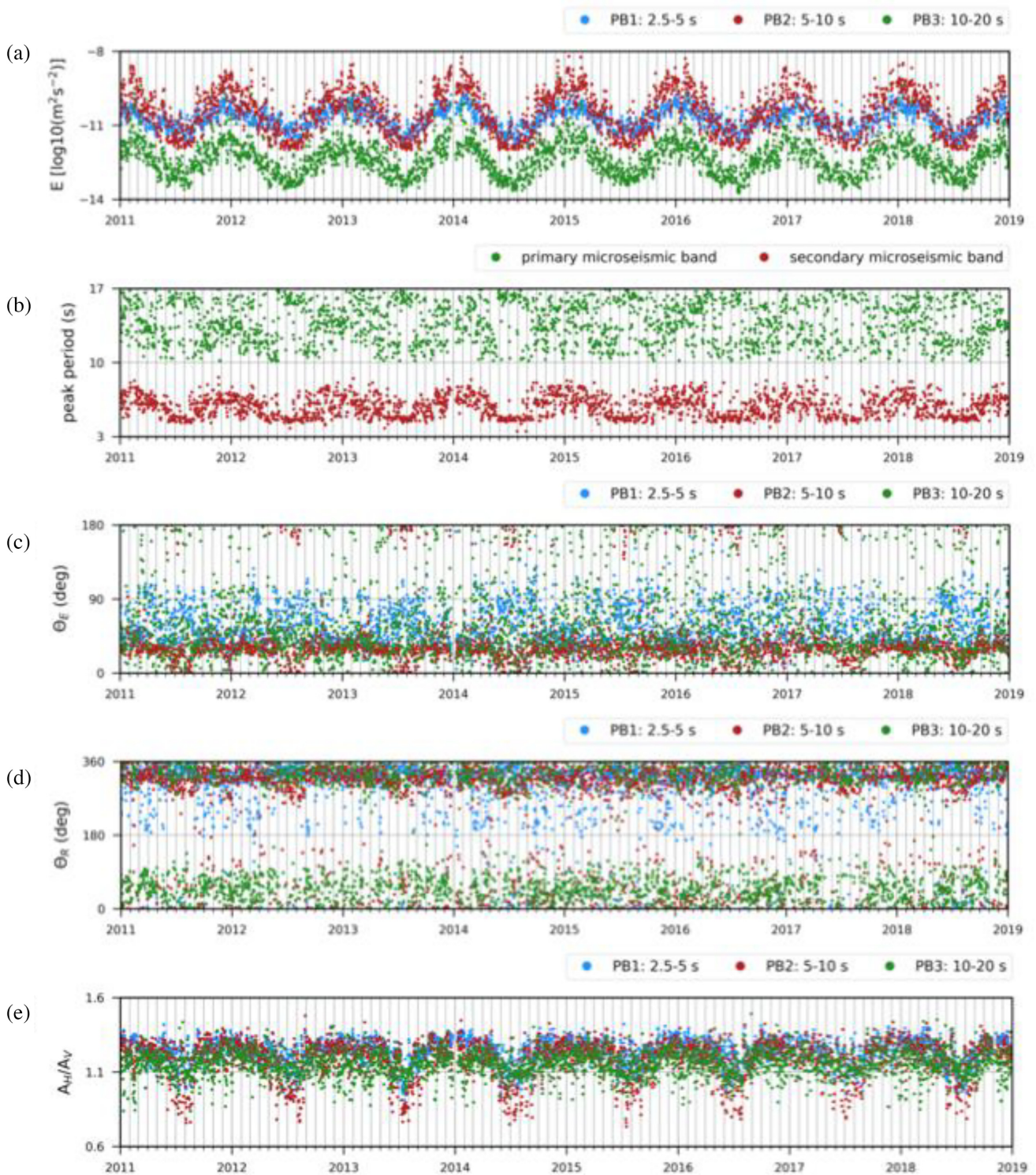


**Figure 2.** Example of analysis for a single station FUSIO of the Switzerland seismic network CH [Switzerland seismic network, Swiss Seismological Service (SED) At ETH, Zurich 1983] located in the centre of the study region. (a)  $E$ , the total energy over three components expressed by velocity with unit  $[\log_{10}(\text{m}^2 \text{s}^{-2})]$ ; (b)  $T_P$  and  $T_S$ , dominant periods of the Primary and Secondary microseismic peaks; (c)  $\theta_E$ , the most energetic horizontal direction of wave propagation; (d)  $\theta_R$ , the dominant horizontal direction of Rayleigh wave propagation; the angle is equivalent to backazimuth for earthquake data, that is, the angle (from north) from which the waves are incoming and (e)  $A_H/A_V$ , the square root of the energy ratio between the horizontal and vertical components. See Section 2 (Data and Data Processing) for detailed definition of each quantity.

neither in our study, nor in the study by Evangelidis & Melis (2012) who analysed the noise spectrum across the Hellenic Network. The behaviour of  $T_P$  and  $T_S$  is a first hint towards the presence of two different source areas for which the relative influence changes through the year (see Section 3).

Due to scatter, propagation directions of  $\theta_E$  and  $\theta_R$  cannot be easily interpreted for single stations. We here show the meaning of the observations in terms of geometrical considerations, to prepare for Section 3.  $\theta_E$ , that is, the direction of dominant energy in the horizontal plane, is, barring scatter, for FUSIO oriented towards  $20^\circ$ – $50^\circ$  north (NNE-NE or SSE-SE), while  $\theta_R$  corresponds to waves incident from NW-NNW, that is, at large angle to  $\theta_E$ . This means that, at the location of FUSIO, the Rayleigh waves do not dominate the horizontal particle motion. Assuming that the source areas for Rayleigh and Love waves are located in the same direction as compared to the seismic station (but not necessarily in the same source area), we have here an indication of Love wave amplitudes dominating over the horizontal component of the Rayleigh waves, coherently with the observations of Friedrich *et al.* (1998) and Juretzek & Hadziioannou (2017).

Finally,  $A_H/A_V$  is almost identical in the three frequency bands, with strong seasonal variations, in particular in PB2. The cause of these variations will be discussed in the Results section. We will in the following present figures that show the spatial variation of the yearly average of the different parameters. In the cases where a given parameter varies over the year, we will also present values for ‘summer’, here defined as May to September, and ‘winter’, defined as November to March.

### 3 RESULTS

In this section, we present the outcome of the data analysis. Each observed parameter has complementary information, in spite of a certain dependency between parameters. The overall noise level  $E$  and the shape of the amplitude spectrum as captured by  $T_P$  and  $T_S$  mainly demonstrate how the seismic noise field in Europe is dominated by two different directions of incoming noise, whose relative significance is dependent on the location, period range and time of year. The relationship between components, as observed through the spatial variations of  $\theta_E$  and  $\theta_R$  and through temporal and spatial variations of  $A_H/A_V$ , informs qualitatively on the wave composition in terms of Rayleigh, Love and body waves.

#### 3.1 Spatial and temporal variations of $E$

$E$  calculated for each day is the median of the sum of the squared amplitudes of the three components. Fig. 3 shows the distribution of  $E$  across Europe, for each period band (left to right). The figure presents at the top the yearly median  $E$  (i.e. for each station the median of all daily values of  $E$ ), the middle row the summer median  $E$  (May to September) over all the days available within these months, and the bottom row the winter median  $E$  (November to March). The colour scale is for each figure adapted such that the centre of the colour scale corresponds to spatial median, indicated in each figure. With this representation, we are able to focus on the spatial variations rather than on the absolute value of  $E$ . Note that the use of the median value over the year (or summer and winter months) for  $E$  means that we favour frequent occurrences, and minimize the impact of extreme events (major storms, earthquakes). The equivalent to Fig. 3, but using temporal mean rather than temporal median

values, is shown in Fig. S2 in the Supporting Information. The use of median versus mean does not alter any of the conclusions below.

A first observation is that the median (over the study area) decrease of the noise level in summer as compared to the yearly average is smaller than the spatial variations across Europe. The yearly medians (Fig. 3, top) demonstrate that the noise level has three main contributions. First, for all period bands, the noise level overall decreases from northwest to southeast, that is, with distance to the northern part of the Atlantic Ocean, with the strongest decrease being in PB2. The overall decrease of total energy  $E$  from NW to SE is related to wave attenuation as the waves propagate away from the areas in the North Atlantic Ocean that generate the seismic noise. We will collectively call these areas the ‘North Atlantic Sources’, without attempting to characterize them other than being located NW of the central part of the study area. The term can therefore cover a variety of different locations, and be different between PB1, PB2 and PB3. As demonstrated by, for example, Arduin *et al.* (2015) and Gualtieri *et al.* (2015), it is the interplay between wave height, wave period, bathymetry and sediments that, combined, generate the seismic noise. We here use the term *Source* to designate areas of noise generation, this, at this combined effect.

Second, there is a significant effect of sources in the eastern Mediterranean Sea in PB1 with an increase of noise amplitudes mainly in Sicily and the Greek Isles. Such effects are negligible in the western part of the Mediterranean Sea. We will therefore call this the ‘East Mediterranean Sources’. Other source areas can be active but over time periods that are of short duration so do not influence the median values over several months or years that we show here. The effect of the East Mediterranean Sources decreases with period, and is insignificant for PB3.

Finally, the main sedimentary basins are, as expected, characterized by high noise levels, with high amplitudes for example (for PB1) in the Aquitaine Basin of southwestern France, in a narrow area located between the Massif Central in France and the Alps (most of it located within the Bresse Graben), the Po Plain, the Molasse Basin and the North German Plain. The effect is almost as strong in PB2, while PB3 has slightly increased amplitudes in only the deepest sedimentary basins (e.g. North German Plain, Po Plain). Note that for PB1 there is a difference between the spatial patterns of the median (Fig. 3) and mean (Fig. S2, Supporting Information) values of  $E$ , with the mean values strengthening the influence of the East Mediterranean Sources. This means that the East Mediterranean Sources can create high noise amplitudes in PB1, over relatively short time periods.

#### 3.2 Spatial and temporal variations of $T_P$ , $T_S$ and the $T_P/T_S$ ratio

Fig. 4 shows  $T_P$ ,  $T_S$  and the  $T_P/T_S$  ratio. Daily  $T_P$  ( $T_S$ ) is calculated as the median value of the period of the local maximum of the vertical component amplitude spectrum within PB3 (PB1–PB2) and daily  $T_P/T_S$  is the ratio between daily  $T_P$  and daily  $T_S$ . As indicated in Section 2, a single source area and waves propagating with constant quality factor for periods around each of  $T_P$  and  $T_S$  would lead to an increase of each of  $T_P$  and  $T_S$  with distance to the source. The  $T_P/T_S$  ratio would be approximately 2, possibly slowly changing with the distance to the source area due to intrinsic wave attenuation. Whether this spatial change would lead to increase or decrease of  $T_P/T_S$  would depend on the quality factor in each of the period bands, and on the precise shape of the spectrum. Scattering of the waves, created by wave interaction with sedimentary basins,

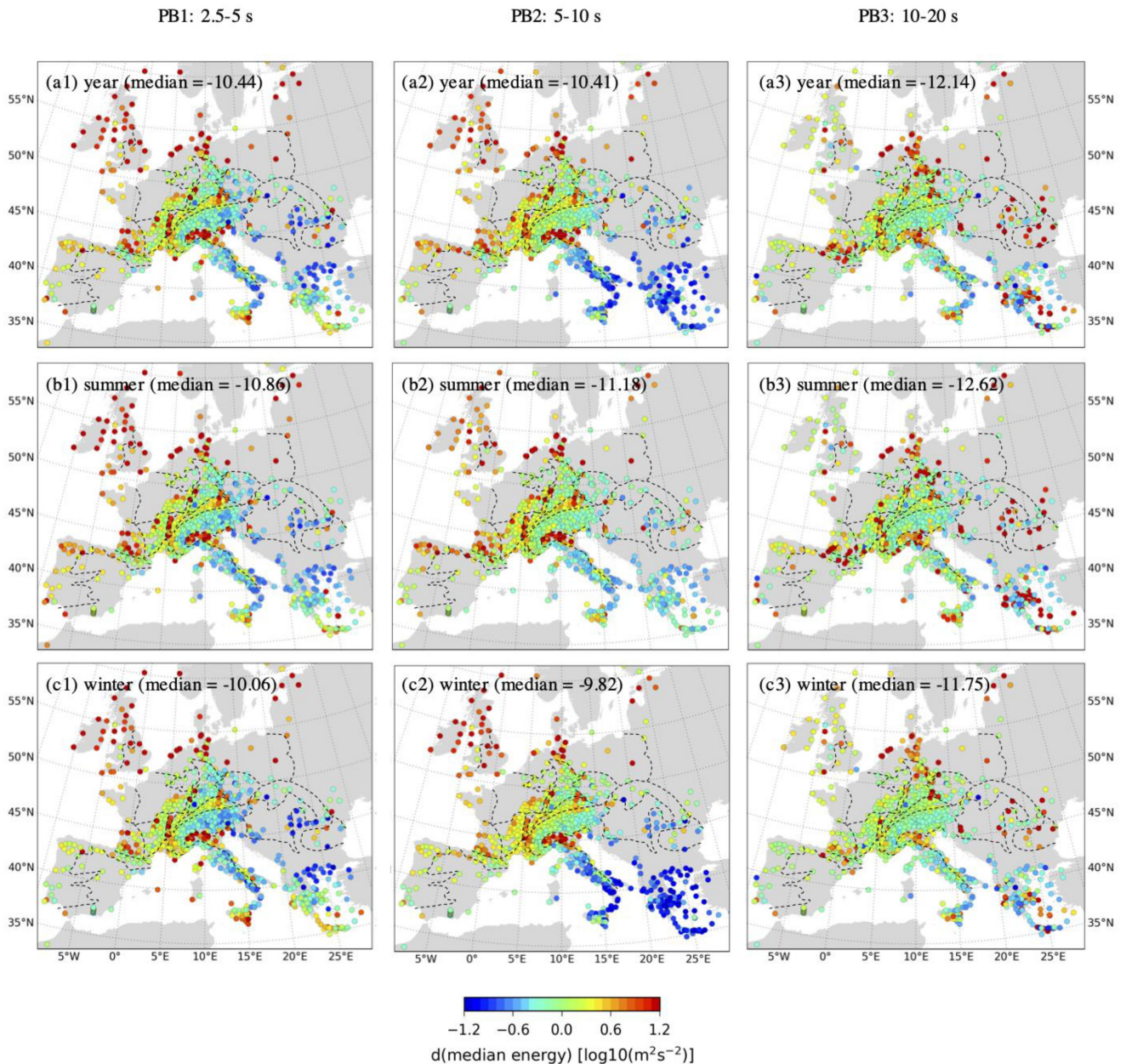


**Figure 3.** Spatial distribution of the median energy ( $E$ ) over the (a1)–(a3) years, (b1)–(b3) summer and (c1)–(c3) winter seasons in three period bands PB1 2.5–5 s (left), PB2 5–10 s (centre) and PB3 10–20 s (right). We display in colour code the variation of this quantity as compared to the spatial median denoted at the top of each subplot. Note that the median value is different between period bands and time period (year, summer and winter). Note also the use of logarithmic scale, as in Fig. 2. The black dashed lines in each subplot correspond to the geological boundaries shown in Fig. 1. See Fig. S2 in Supporting Information for the spatial distribution of the energy ( $E$ ) calculated as temporal mean (rather than temporal median).

multiple scale crustal heterogeneities and mountains, in particular the Alps, also influences  $T_P$  and  $T_S$  independently. Due to these large-scale tectonic differences, the scattering characteristics vary spatially across Europe with, in general, strong scattering at short periods (PB1 and PB2) and low to moderate scattering at longer periods (PB3), depending on crustal heterogeneity.

The behaviour of  $T_P$  is coherent with a dominant influence by only the North Atlantic Sources, with  $T_P$  increasing from northwest to southeast. There is no significant influence by the East Mediterranean Sources in  $T_P$ : if a strong source characterized by shorter periods were present, we would expect a shift towards shorter periods of  $T_P$  near the Mediterranean Sea, especially in summer; this

is not observed. Therefore, there is neither in  $E$ , nor in  $T_P$  any indication of a sufficiently strong contribution of the East Mediterranean Sources (or any other Mediterranean sources) to significantly shift the Primary microseismic peak. As discussed in the previous section, the Primary microseismic peak of the East Mediterranean Sources may be present, but it is not sufficiently strong to be identified as a local maximum in the spectrum. This holds true throughout the year. However, the spatial contrasts are stronger in summer than in winter, because the NW part of the study area sees an increase in  $T_P$  from summer to winter, while the stations close to the eastern Mediterranean Sea shows a decrease of  $T_P$  from summer to winter.

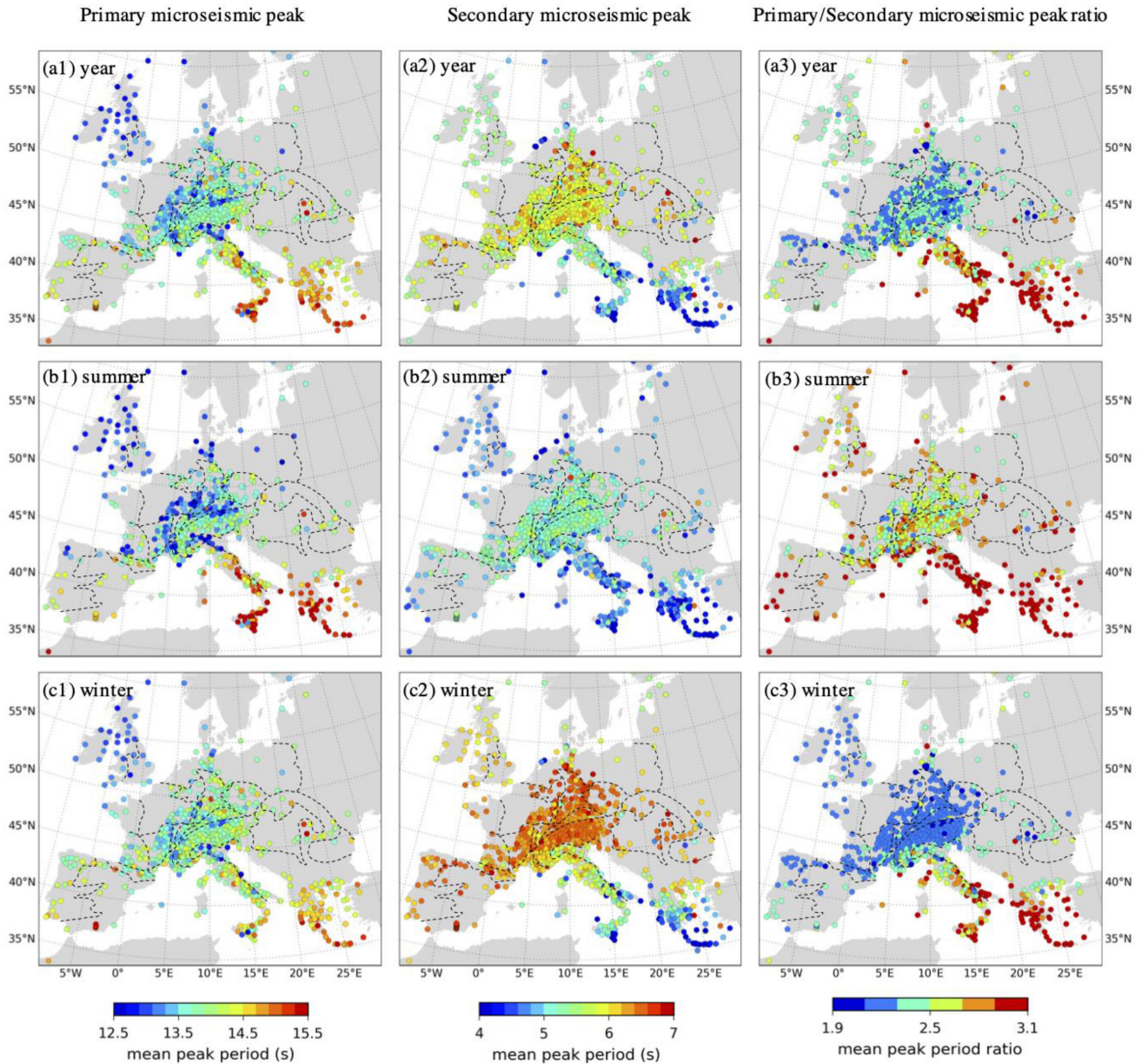


**Figure 4.** Spatial distribution of quantities related to the dominant periods of the Primary ( $T_P$ ) and Secondary ( $T_S$ ) microseismic peaks. We show the average  $T_P$ ,  $T_S$ ,  $T_P/T_S$  over the (a1)–(a3) years, (b1)–(b3) summer and (c1)–(c3) winter periods. The black dashed lines in each subplot correspond to the geological boundaries shown in Fig. 1.

$T_S$  has a fundamentally different behaviour. For the average across the year,  $T_S$  increases from approximately 5.5 s in the British Isles to approximately 6 s towards the Alps. Further southeast, the period decreases again, to below 5 s, in Italy and Greece. The same increase–decrease pattern is observed separately in summer and winter with a shift towards shorter periods in summer and longer periods in winter. This pattern is a clear indication of the simultaneous influence from the North Atlantic Sources and the East Mediterranean Sources, with the effect being higher on  $T_S$  than on  $E$  (see Fig. 3).

Because of the different variations of  $T_P$  and  $T_S$  across the study area, the  $T_P/T_S$  ratio shows significant lateral variations. Note that scatter in either  $T_P$  or  $T_S$  results in strong scatter of  $T_P/T_S$  so only major trends should be considered. Over the whole year,  $T_P/T_S$  is

within the range of 2.1–2.5 in all of the western and northern parts of the study area, including the Alps, northern Italy and France. With the quite high  $T_P/T_S$  ratio, one can speculate that there may be two source areas even though they would be located in the same direction with respect to the study area. The  $T_P/T_S$  ratio increases towards the SE within the Italian peninsular, with a ratio higher than 3 in Sicily and much of Greece, indicative that the relative influence of different source areas changes spatially. This is coherent with (and the consequence of) the observations of  $T_P$  and  $T_S$  (see above). In summer,  $T_P/T_S$  increases overall, so the areas with very high  $T_P/T_S$  increase in size and the average value north and west of the Italian peninsular increases by 0.1–0.3. The opposite effect takes place in winter. It is remarkable that the theoretical ratio of approximately 2 (darkest blue range, 1.9–2.1), indicative of the same source area

contributing to the noise, is only present in winter in the north and western part of the study area, and only sporadically for the yearly average values.

So also with  $T_P$  and  $T_S$  measurements, we observe that the noise field in Europe is the result of competing influences of the North Atlantic Sources and the East Mediterranean Sources. The latter have a major influence on the Secondary microseismic peak (decreasing  $T_S$  in the eastern part of the study area) and only a minor, if any, influence on the Primary microseismic peak.

The spectra that we observe do not split into two distinct peaks as observed in some studies (e.g. Bromirski *et al.* 2005); we rather observe subtle and continuous variations over space, time and frequency. With source regions in two distinct directions, we can however conclude that the different source areas have different dominant frequencies of the Secondary microseismic peak, coherent with the hypothesis of different sources areas being the cause of the splitting of the Secondary microseismic peak (e.g. Koper & Burlacu 2015).

### 3.3 Spatial and temporal variations of $\theta_E$ and $\theta_R$

The measurements of  $\theta_E$  (horizontal direction with the highest energy) and  $\theta_R$  (horizontal direction which is the closest to a  $90^\circ$  phase shift with the vertical component) are inherently more subject to random noise than the previous observations. We therefore show only results for the part of the study area where we have the highest station density. Fig. 5 shows the yearly values of  $\theta_E$  and  $\theta_R$  in each of the three period bands, and the histograms of the angular difference. In each map, we also show the rose diagram of the directions over all stations. The azimuth uncertainty, calculated as the standard deviation of daily measurements, is  $15^\circ$ – $20^\circ$  at most stations. These high values of uncertainty has two causes: the measurements are somewhat unstable, and there are significant differences in propagation pattern and wavefield between different days. There is no apparent spatial pattern of the uncertainties (see Figs S4 and S6, Supporting Information).

With the exception of a few locations,  $\theta_E$  and  $\theta_R$  only have small to moderate variations over the year (see Figs S3 and S5 in the Supporting Information for observations in summer and winter). Changes over the year in the angular differences between  $\theta_E$  and  $\theta_R$  are absent in PB3, and small in PB1 and PB2, with the difference relatively to the yearly value increasing in summer by  $3^\circ$  (median value in PB1) and  $5^\circ$  (median value in PB2) and decreasing in winter by  $2^\circ$  (PB1 and PB2).

Note that the wide spread in  $A_L/A_R$  values for PB1 (see Fig. 6 and associated discussion) means that our maps of  $\theta_E$  and  $\theta_R$  in PB1 should be interpreted with caution.

Fig. 5 shows that the angular difference between  $\theta_E$  and  $\theta_R$  is high (median values between  $70^\circ$  and  $76^\circ$ ). This observation implies that the Love waves are of higher amplitude on the horizontal components than the Rayleigh waves, and that the source areas for Rayleigh and Love waves are located in the same directions. Therefore, while  $\theta_R$  indicates the approximate propagation direction of the Rayleigh waves,  $\theta_E$  is in most points associated with Love waves, and perpendicular to the propagation direction. This observation does not fully hold true in PB1 (see discussion of Fig. 6 below), for which the maps of  $\theta_E$  in some cases are likely to be associated with Rayleigh waves.

The maps show that PB3 has the simplest spatial patterns of  $\theta_E$  and  $\theta_R$  with dominance of sources towards NW-NNW, as expected. In many locations, the direction changes abruptly and/or the observations have more scattered directions when the waves enter

the Alps. For PB3, the surface waves have wavelengths of up to 50 km so they are influenced mainly by the upper crust, but have some sensitivity to the crust as a whole, therefore being sensitive to Moho thickening, for example. Significant wave conversions between Rayleigh and Love waves, as well as between modes, can take place, so it is not justified to interpret the propagation directions as a simple propagating wavefront. One should rather consider that significant scattering is taking place as soon as the waves enter the Alps, and that the wavefield is complex both within, and southeast of the Alps. Similar phenomena are observed in PB2 and PB1. While directions change over short distances both in PB1 and PB2, there is still a link to the crustal structure, with for example propagation directions perpendicular to the basin edges of the Po Plain, which may be an indication of trapped waves propagating back and forth between the basin edges. The complexity of the wavefield in PB1 and PB2 lead to rose diagrams where the incoming wave direction from NW and SE is no longer dominant. Additionally, the direction of  $\theta_E$  and  $\theta_R$  are in many locations similar in PB1, so the interpretation of the  $\theta_E$  and  $\theta_R$  in PB1 is difficult. We do not see, within this part of the study area, a reversal of propagation directions in PB1 and PB2 so while the Eastern Mediterranean sources influence the noise significantly, propagation directions remain dominated by waves from the North Atlantic Ocean. Looking at stations in southern Italy and Greece (not shown here), we observe a significant difference in the rose diagrams between summer and winter, demonstrating more diverse source contributions, but the station density is not sufficient to provide reliable maps.

Our results complement those of Juretzek & Hadziioannou (2016). They could obtain more rich information at a few selected locations, using array analysis. Therefore, they could study the distribution of arrival directions at the array, where we on the contrary extract only the dominant one, but with a better spatial coverage. It is difficult to directly compare the outcome of the two studies (our Fig. 5, their fig. 4), but the dominant directions agree at the common locations, and the diversity of directions (or lack of diversity) that Juretzek and Hadziioannou show are reflected in the spatial variations that we observe around their observation points. Juretzek & Hadziioannou (2016) conclude that Love wave energy generally dominates over Rayleigh wave energy, which is in agreement with our observed angular difference of approximately  $90^\circ$ .

Calculating the ratio  $A_L/A_R$  between the amplitude in the horizontal direction parallel to and perpendicular to  $\theta_R$  gives us a proxy for the relative horizontal amplitude of the two wave types. The total energy ratio between modes or wave types can be calculated integrating kinetic energy over depth using a known displacement amplitude at the surface and an earth model (e.g. Nishida *et al.* 2008; Juretzek & Hadziioannou 2016), but this calculation is not possible in our case because array processing is required for the wave separation. The fact that  $\theta_E$  and  $\theta_R$  are not only different, but dominantly perpendicular, can be explained by Love and Rayleigh waves from a single source direction, and amplitudes of Love waves being higher than the horizontal component of the Rayleigh waves.  $A_L/A_R$  does however remain a proxy, as this simple explanation does not capture multiple source directions and scattering. Both of these effects would lead to  $A_L$  including some Rayleigh wave energy and  $A_R$  including some Love wave energy. The spatial distribution of  $A_L/A_R$  is shown in Fig. 6, with a histogram of the ratios shown in the upper left corner of each subplot. There is significant spatial scatter, related to the difficulty of obtaining stable measurements, so the ratio at a single station is not significant. The colour shift between the different frequency bands demonstrates that the Love wave dominance on the horizontal component increases from PB1 (where the

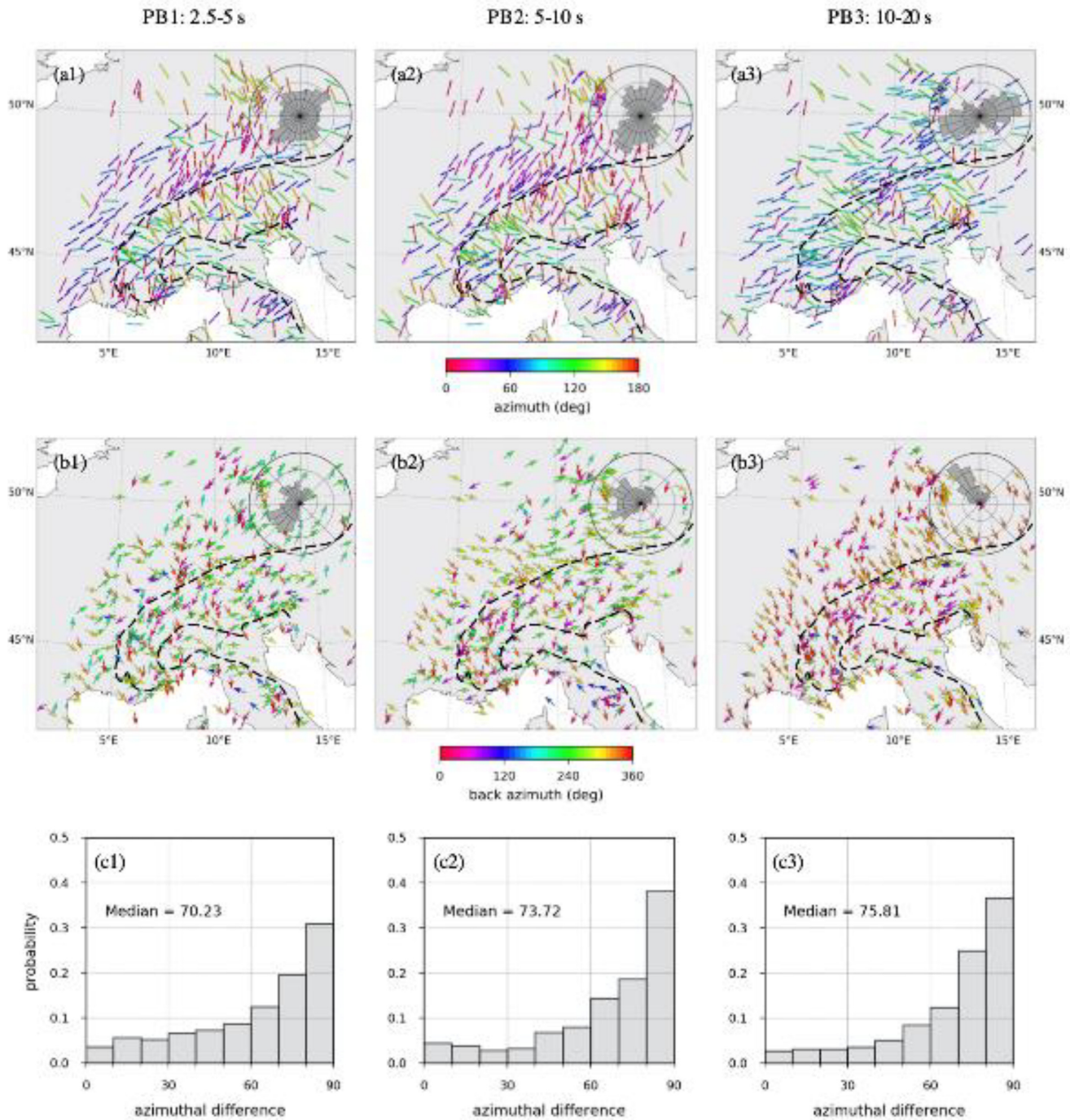


**Figure 5.** Spatial distribution of quantities related to the most energetic horizontal direction of wave propagation ( $\theta_E$ ), and the dominant horizontal direction of Rayleigh wave propagation ( $\theta_R$ ) for each period band (left: PB1 2.5–5 s; centre: PB2 5–10 s and right: PB3 10–20 s) in the central part of the study area. The colour scales repeat the information on propagation directions (indicated by lines for  $\theta_E$  and arrows for  $\theta_R$ ), to increase clarity. Top row (a1)–(a3): yearly average values of  $\theta_E$ . Centre row (b1)–(b3): yearly mean values of  $\theta_R$ . The rose diagram in the top right corner of each subplot displays the statistics over all stations. Note that for  $\theta_R$ , the colour scale and the rose diagram indicates direction from which the waves are incoming. The black dashed lines in each subplot are simplified geological boundaries from Fig. 1, included to emphasize geological structures discussed in the main text. The equivalent plots for summer and winter are shown in Figs S3 and S5 in the Supporting Information. Bottom row (c1)–(c3): histograms of angular differences between  $\theta_E$  and  $\theta_R$ .

median value of the ratios is approximately 1.05 but with a broad distribution) through PB2 (with a median ratio of 1.06 and a more narrow distribution of values generally higher than 1) to PB3 (with a median value of 1.12 and almost all values higher than 1). There is no significant variation of these ratios between summer and winter

(not shown), in agreement with Juretzek & Hadziioannou (2016). Our results contradict those of Tanimoto *et al.* (2016) who concluded on an increase in the Rayleigh to Love wave energy during the summer months. The mismatch would be explained by our observation that the vertical component is significantly influenced by  $P$

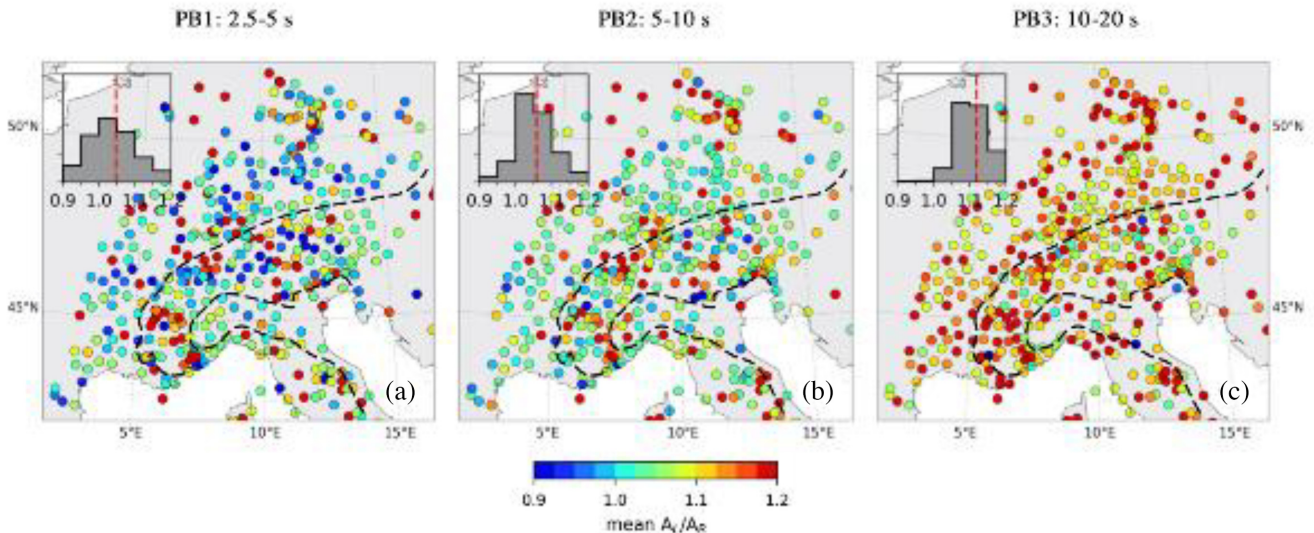


**Figure 6.** Properties of the average Love to Rayleigh amplitude ratio ( $A_L/A_R$ ) over the years in three period bands PB1 2.5–5 s (left), PB2 5–10 s (centre), and PB3 10–20 s (right). In each subplot, we show the statistics of  $A_L/A_R$  in the top left corner, and the red dashed line indicates the median value. The black dashed lines in each subplot are simplified from the geological boundaries shown in Fig. 1 to emphasize geological structures discussed in the main text as, for example, the Alps and the Po plain.

waves in summer (see the next section), an effect not accounted for by Tanimoto *et al.* (2016), who assumed that the vertical component was dominated by fundamental mode Rayleigh waves.

Fig. 7 shows spatially smoothed values of  $\theta_E$  and  $\theta_R$ . The smoothed versions of  $\theta_E$  and  $\theta_R$  were obtained by averaging measurements in a sliding window of size  $1^\circ \times 1^\circ$  with a lateral step of  $0.33^\circ$  in latitude and longitude (slightly varying with latitude). We keep an averaged measurement only if there are more than three stations in the sliding window. The smoothed images should be interpreted with care, due to the uneven spatial distribution of the initial data points. The major influence of the Alps on the propagation patterns of the surface waves are however well illustrated by the abrupt change of propagation directions in the Alps in PB2, and a mixed situation in PB3. While interpretations are particularly delicate in PB1, where scattering is strong, large-scale coherence of observations demonstrates the major influence of the Alps and of the crustal structure in general on the noise field. There may also be an indication of noise sources in the Baltic Sea in PB1 (see also Lepore & Grad 2018).

Scattering of surface waves in the Alps at 30 s period, that is, close to PB3, has been observed by Cotte *et al.* (2000). They documented that surface wave propagation directions in the western Alps were up to  $30^\circ$  different from the direction of the great circle for teleseismic events, with at least half of that difference due to the Alpine crustal structure. Stich & Morelli (2007) and Stich *et al.* (2009) also observed and modelled strong effects from the Alpine crustal structure in that period range. The Alps (for a recent model covering our study area, see the full waveform inversion by Lu *et al.* 2020) are characterized by strong Moho topography and a fully 3-D geometry. Scattering and wave deviations at long periods due to crustal structure will occur also at relatively long periods, as Moho reaches a depth of 65 km depth in the model by Lu *et al.* (2020) and 80 km according to the receiver function study by Zhao *et al.* (2015). As frequency increases (i.e. moving from PB3 to PB1), the influence of the local crustal structure can be expected to play an increasing role, so that the propagation patterns will potentially change over short distances, in agreement with our observations. This increase of

scattering with frequency would tend to render the wavefield more diffuse, but the coherent geographical patterns of the polarization analysis shows that the wavefield retains a significant deterministic part.

The complexity of the wavefield created by the scattering, especially in PB1 and PB2, may explain why the Green's function in noise correlations converges well in Europe both for Rayleigh waves (e.g. Kästle *et al.* 2018; Lu *et al.* 2018, for AlpArray) and Love waves (Alder *et al.* 2021), in spite of very dominant noise sources from only a few source areas. Our results also show that the convergence rate may be dependent on both frequency and geographical location within Europe. Caution must also be taken for the extraction of Rayleigh and Love waves on the horizontal components: the strong scattering and complex wave propagation mean that it may not be valid to separate the Rayleigh and Love waves on the horizontal components of the noise correlations by rotation into RR and TT components.

### 3.4 Spatial and temporal variations of $A_H/A_V$

Fig. 8 shows the yearly averages, for each frequency band, of  $A_H/A_V$ , that is, the square root of the energy ratio between horizontal and vertical components. Note that  $A_H/A_V$  uses both horizontal components, with a mix of Rayleigh and Love waves, so  $A_H/A_V$  cannot be directly used to deduce earth structure. Variations in  $A_H/A_V$  will however be impacted by the Rayleigh wave fundamental mode  $H/V$  ratio and, consequently, the local structure is the main dominant influence on  $A_H/A_V$ . The ratio of horizontal to vertical component amplitudes has been used for decades to characterize earth structure (Nakamura 1989), with the  $H/V$  ratio being related to the (frequency dependent) surface wave modal eigenfunctions. The simulations by Tanimoto *et al.* (2006, figs 11 and 12) show that for the period band considered here, the horizontal to vertical amplitude of fundamental mode Rayleigh waves increases when the shear velocity close to the surface decreases. This is coherent with our observations. In PB1, all major and minor sedimentary basins are characterized by high  $A_H/A_V$ . As the periods become longer, the minor and/or less deep

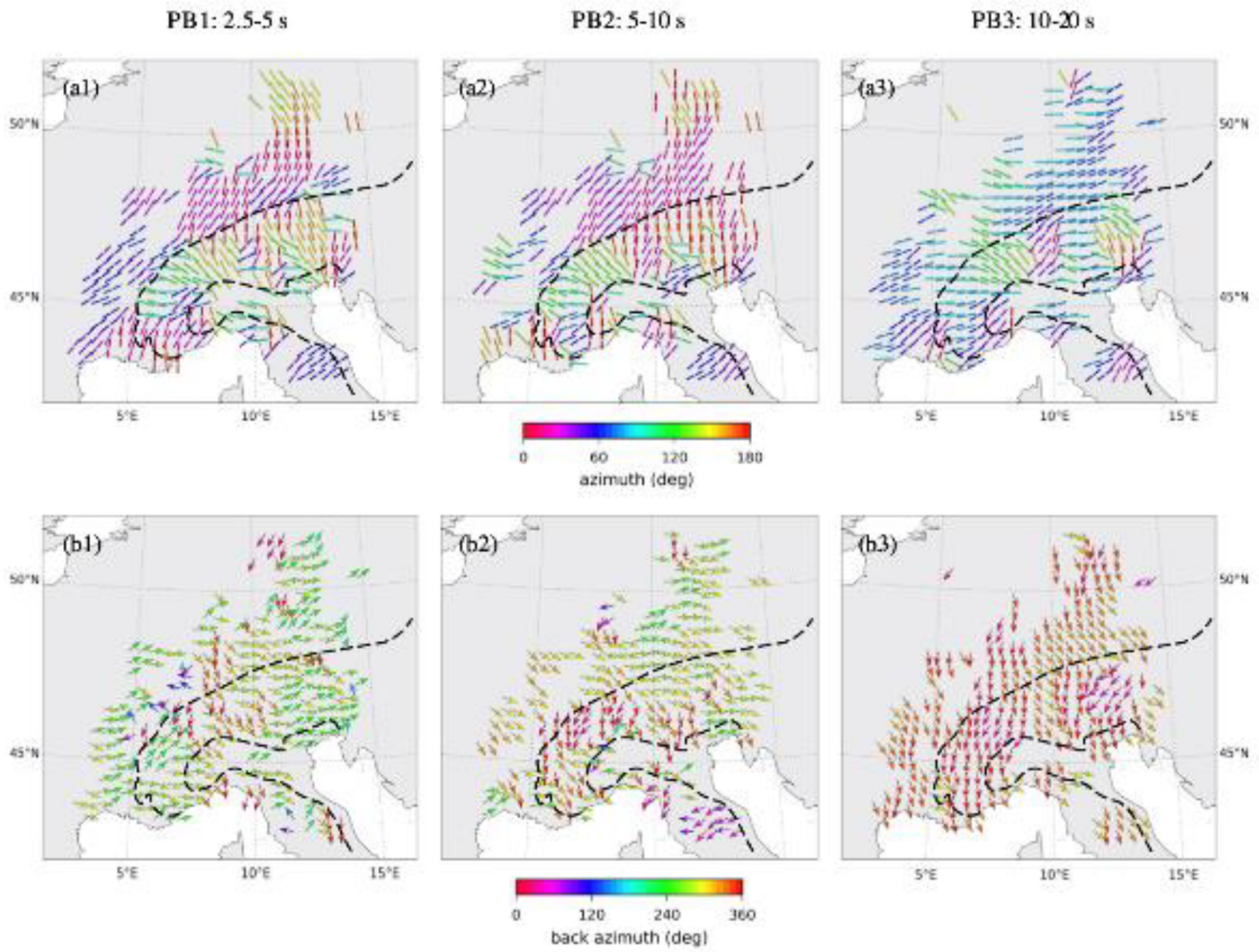


**Figure 7.** Spatially smoothed values of  $\theta_E$  (top) and  $\theta_R$  (bottom) in the three period bands 2.5–5 s (left), 5–10 s (centre) and 10–20 s (right).

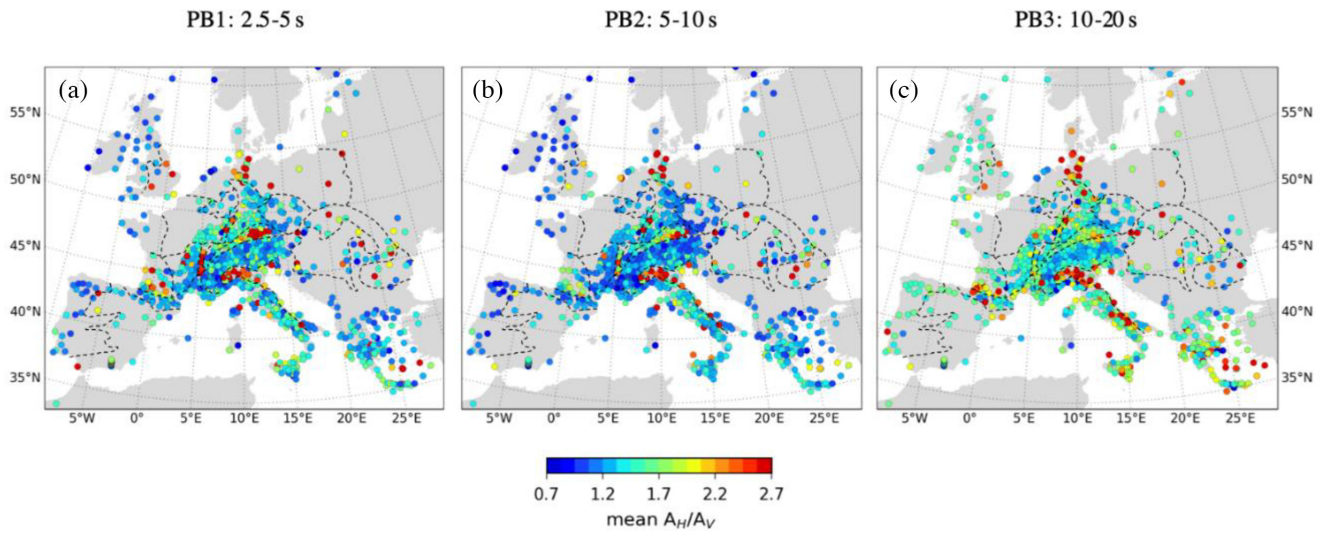


**Figure 8.** Spatial distribution of the average square root of the energy ratio between horizontal and vertical components ( $A_H/A_V$ ) over the years in three period bands PB1 2.5–5 s (left), PB2 5–10 s (centre) and PB3 10–20 s (right). The black dashed lines in each subplot correspond to the geological boundaries shown in Fig. 1.

basins become less prominent (e.g. Bresse Graben, Molasse Basin). In PB3, only the Po Plain and the North German Plain stand out with high  $A_H/A_V$ . The crustal structure as a whole influences  $A_H/A_V$ , especially at long periods, and the Alps are clearly identifiable in PB3, with low  $A_H/A_V$  as compared to surrounding areas.

The  $A_H/A_V$  dependency on crustal structure is classic, and in our study not of any main interest, as wave separation using array analysis is needed to exploit  $A_H/A_V$  to invert for earth structure. The remainder of this section is dedicated to the insights into the wavefield that can be obtained by the variations of  $A_H/A_V$  that occur over the year. As there is no significant change in the relative ratio of Love to Rayleigh waves over the year (see previous section), one can at this stage hypothesize that a change of relative influence of surface waves and body waves through the year could be detected by variations in  $A_H/A_V$ .

There are indeed significant variations in  $A_H/A_V$  over the year, even though they are smaller than the spatial variations. Fig. 9 shows at the top variations in  $A_H/A_V$  in PB2 over all the years and across three different networks: GB (Great Britain Seismograph Network), CH (Switzerland seismic network, Swiss Seismological Service (SED) at ETH 1983) and HL (National Observatory of Athens Seismic Network, National Observatory of Athens, I.O.G., 1997). These average network values demonstrate a clear decrease of  $A_H/A_V$  over summer as compared to the average of the year for networks CH and HL, and an insignificant summer decrease for GB, located on the edge of the North Atlantic Ocean. Fig. 9 also shows (bottom) the variations in  $A_H/A_V$  for network CH, in each of the three period bands PB1–PB3, showing that the seasonal variations of  $A_H/A_V$  are strongest in PB2.

The analysis, in PB2, of the particle motion rectilinearity (Flinn 1965), that is, the degree to which the particle movement is linear, shows that when  $A_H/A_V$  decreases, the rectilinearity increases. A working hypothesis at this stage is that the relative amount of (sub-)vertical  $P$  waves increases as compared to the amount of surface waves. This hypothesis is coherent with the maximum effect being in PB2, a period band for which there are many observations of teleseismic body waves (e.g. Gerstoft *et al.* 2008) and potential for global imaging with seismic noise correlations (e.g. Boué *et al.* 2013).

To further understand how  $A_H/A_V$  variations over time give insight into the wavefield composition, we perform  $f$ – $k$  analysis of the noise field using the CH network. Fig. 10 shows two examples of such analysis, for two different days in 2018 September. The  $f$ – $k$  analysis is based on the classical plane-wave beamforming algorithm as described in Rost & Thomas (2002). We calculate beam power using different wave slowness and azimuth. The computation is carried out in the frequency domain for each 10-min segment of the  $Z$ -component daily recordings, of which the median values in each (azimuth, slowness) pixel are used to form the daily beamforming result. For each daily sum we normalize the plot to a maximum of one.

As shown in Fig. 10, on September 19, there were major wave heights in both the Southern Hemisphere and in the North Atlantic Ocean. The average  $A_H/A_V$  in PB2 for network CH on that day is typical for days with storms in the North Atlantic Ocean, with  $A_H/A_V$  13 per cent higher than the yearly average (see Fig. 11, which shows  $A_H/A_V$  in PB2 for CH during 2018). The  $f$ – $k$  plot in Fig. 10 shows energy incoming from WNW, with a wave slowness of  $0.35 \text{ s km}^{-1}$ , that is, with velocities indicative of surface waves. These surface waves dominate the  $f$ – $k$  plot, so contributions from the Southern Hemisphere storms are not visible. On September 6, the wave heights in the Southern Hemisphere were overall less, but there

are still significant waves in the area of the  $f$ – $k$  plot corresponding to PKP waves (slowness  $< 0.05 \text{ s km}^{-1}$ , see Fig. S7 in the Supporting Information for a slowness-distance plot of PKP waves). In the absence of significant activity in the North Atlantic Ocean, the  $f$ – $k$  analysis is dominated by subvertical  $P$  waves, and  $A_H/A_V$  (see Fig. 11) is approximately 15 per cent less than the yearly average (from 1.21 to 1.03). These observations show that while  $A_H/A_V$  is indicative of local crustal structure, the variations of  $A_H/A_V$  over time is indicative of the relative amount of subvertical  $P$  waves as compared to surface waves. This double dependency on  $P$  and surface waves can be captured by a quantity that we call Beampower Ratio. We define this entity as the ratio between the cumulated beam power of surface waves (summing the beam power of the area corresponding to velocity range  $2.5$ – $5 \text{ km s}^{-1}$ ) and that of subvertical  $P$  and surface waves (summing the beampower of the area with velocity  $> 20 \text{ km s}^{-1}$  and the area corresponding to the range  $2.5$ – $5 \text{ km s}^{-1}$ ).

Fig. 11 shows the comparison of the average  $A_H/A_V$  across the CH network with the Beampower Ratio during 2018. The variations of the two are in excellent agreement. We therefore argue that the difference of  $A_H/A_V$  in summer as compared to the yearly average can be used as a proxy to map the relative strength of  $P$  waves within the noise field as compared to the surface waves. We here provide a simple explanation why the variations of Beampower Ratio, calculated on the vertical component, mimic those of  $A_H/A_V$ .

We assume that the noise wavefield is dominated by surface,  $P$  and PKP waves, which could contribute to both horizontal and vertical components of seismic recordings. Thus,  $A_H/A_V$  can be expressed as a sum of the energy of horizontal and vertical components of these three phases (see our definition of  $A_H/A_V$  in Section 2, Data and Data Processing):

$$\frac{A_H}{A_V} = \sqrt{\frac{E_H}{E_V}} = \sqrt{\frac{E_{H(\text{surface})} + E_{H(P)} + E_{H(\text{PKP})}}{E_{V(\text{surface})} + E_{V(P)} + E_{V(\text{PKP})}}}$$

While the PKP waves are mostly generated from the far-field sources (with great circle distance  $> 155^\circ$ , see Fig. S7 in the Supporting Information and see areas enclosed by green lines in the Southern Hemisphere in Figs 10 b and d), the  $P$  waves are more likely to share the same source origins as the surface waves, that is, the North Atlantic Sources and East Mediterranean Sources (with great circle distance in the range  $15^\circ$ – $60^\circ$ ). The  $P$  waves would have incidence angles  $< 40^\circ$ , which indicate higher contribution to the vertical than to horizontal components. However, with the assumption of same source origins, the energy of  $P$  and surface waves will vary (both increase or decrease) simultaneously. If we assume the energy of the  $P$  waves is significantly smaller than that of the surface waves, we can neglect these terms in the equation. With incidence angles  $< 15^\circ$ , the PKP waves mostly contribute to the vertical component, so we ignore their influence on  $E_H$ . Thus, under these assumptions, we can simplify the expression of  $A_H/A_V$  to:

$$\frac{A_H}{A_V} \cong \sqrt{\frac{E_{H(\text{surface})}}{E_{V(\text{surface})} + E_{V(\text{PKP})}}}$$

This expression is further simplified by assuming a constant energy ratio between the horizontal and vertical component surface waves (see previous subsection):

$$\frac{A_H}{A_V} \cong \sqrt{\frac{\alpha E_{V(\text{surface})}}{E_{V(\text{surface})} + E_{V(\text{PKP})}}} = \sqrt{\alpha} \sqrt{\frac{E_{V(\text{surface})}}{E_{V(\text{surface})} + E_{V(\text{PKP})}}}$$

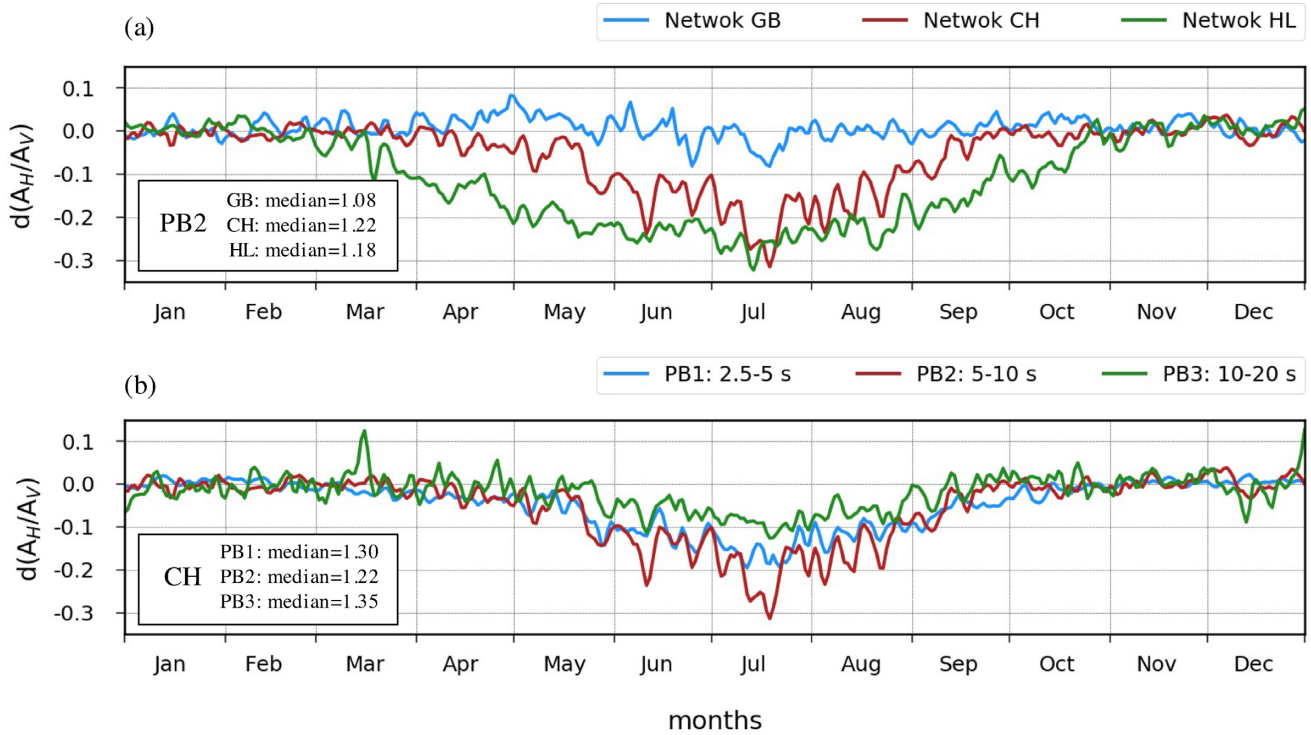


**Figure 9.** The average temporal variation of  $A_H/A_V$  over the years for (a) three networks in PB2: GB (the Great Britain Seismograph Network, British Geological Survey 1970), CH (Switzerland seismic network, Swiss Seismological Service (SED) at ETH 1983) and HL (National Observatory of Athens Seismic Network, National Observatory of Athens, I.O.G. 1999) and (b) network CH in three period bands PB1 2.5–5 s, PB2 5–10 s and PB3 10–20 s. We display the relative variation of  $A_H/A_V$  to the winter median as denoted in the bottom left corner of each subplot.

with

$$\alpha = \frac{E_{H(\text{surface})}}{E_{V(\text{surface})}}$$

As the surface waves are a mix of Rayleigh and Love waves, and both are influenced by the local crustal structure,  $\alpha$  cannot be interpreted in terms of earth model or relative contributions of Rayleigh or Love waves. However,  $\alpha$  is unlikely to vary significantly over the year (see end of subsection Spatial and temporal variations of  $\theta_E$  and  $\theta_R$ ).

By calculating, the ratio of the total beam energy (using the vertical component of motion) for slownesses associated with surface waves and the total beam energy associated with surface waves and PKP waves, we therefore obtain a proxy to  $A_H/A_V$ :

$$\frac{A_H}{A_V} \sim \frac{\text{Beampower}_{V(\text{surface})}}{\text{Beampower}_{V(\text{surface})} + \text{Beampower}_{V(\text{PKP})}}$$

Note that the Beampower Ratio only captures *variations* of  $A_H/A_V$ , rather than its absolute value.

Based on the excellent agreement between variations in  $A_H/A_V$  and Beampower Ratio, we argue that changes in  $A_H/A_V$  over time is indicative in changes in wavefield and, more precisely, indicative of the relative amounts of PKP and surface waves, even though these  $A_H/A_V$  variations are only qualitative indications rather than quantitative estimates.

We additionally verified that variations in  $A_H/A_V$  were not related to earthquakes, by checking whether major earthquakes had any systematic influence (increase, decrease) of  $A_H/A_V$ . Even major earthquakes, with magnitude  $>7$  did not have a any noticeable influence on  $A_H/A_V$  (see Fig. S8 in the Supporting Information).

Fig. 12 shows the difference between the average  $A_H/A_V$  in winter

and in summer, in the three period bands. We observe that in PB3, there are (barring data scatter) no significant variations of  $A_H/A_V$  during the year. On the contrary, there is a strong spatial dependency of the seasonal variation of  $A_H/A_V$  in PB1 and PB2. In PB1, the effect of a summer decrease of  $A_H/A_V$  starts at longitude approximately  $10^\circ\text{E}$ , with the exception of Sicily and the Greek Isles. The same pattern is present in PB2, with strong decreases of  $A_H/A_V$  in summer around the Mediterranean, and only a limited effect north of Latitude  $45^\circ\text{N}$ . Overall, the effect is stronger in PB2 than in PB1.

Our results show that sub-vertically propagating  $P$  waves strongly contribute to the seasonal variations in  $A_H/A_V$ , with particularly low  $A_H/A_V$  on days with low wave activity in the Atlantic Ocean and high wave activity in the Southern Hemisphere.

## 4 DISCUSSION AND CONCLUSIONS

This work has the scope of characterizing the noise field in Europe on a large scale, using single-station measurements. The parameters are relatively simple and can be calculated over large data sets, covering many years of data and a large number of seismic stations. Even though the parameters have a certain level of inter-dependency (only three independent observables, each a function of time and frequency), each of them has the potential of informing on specific features of the wavefield. In this study, we specifically targeted the characterization of the noise that dominates over the day and over long time periods (summer, winter or year), by excluding time windows with high amplitude noise and by favouring the use of the median value of each parameter rather than the mean for the calculation of daily, seasonal and yearly values. Focusing on dominant values has the advantage of providing stable parameters in spite of

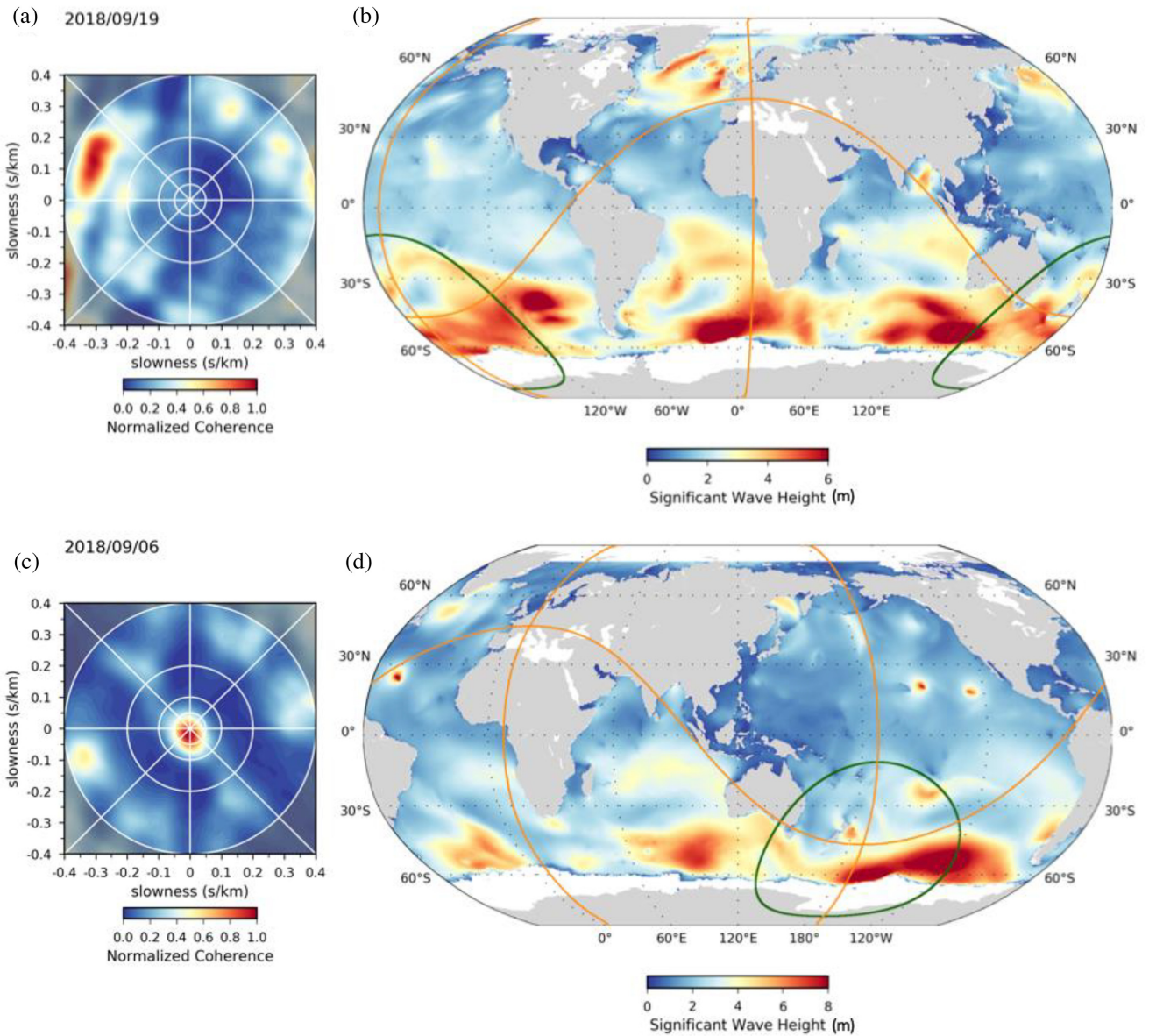


**Figure 10.** Location of major noise sources of September 19 (top) and 6 (bottom) 2018, using beamforming with network CH [Switzerland seismic network, Swiss Seismological Service (SED) at ETH 1983]. (a) and (c) Slowness versus back-azimuth representation of the daily median beamforming results. (b) and (d) Daily median ocean wave height from NOAA operational model archive and distribution system (NOMADS) based on WAVEWATCH III output. Localized typhoons appear as individual small red spots. The orange lines represent shooting great circles along meridian and parallel directions from the network CH. The green lines enclose the area where the excitation of PKP phase could reach network CH. It is computed using the  $\tau$ - $p$  traveltime calculation functionality (Crotwell *et al.* 1999) of Obspy using on the 1-D global Earth model IASP91 (Kennett & Engdahl 1991).

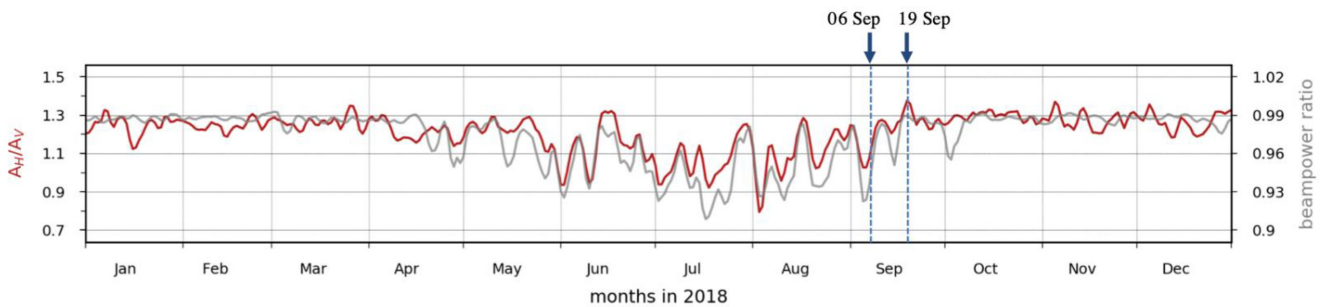


**Figure 11.** Comparison between the  $A_H/A_V$  and Beampower Ratio in 2018 for network CH. The Beampower Ratio refers to the ratio between the cumulated beam power of surface waves (area with velocity in the range  $2.5\text{--}5\text{ km s}^{-1}$ ) and the cumulated beam power of surface and teleseismic body waves (summing the beampower of the area with velocity  $>20\text{ km s}^{-1}$  and the area corresponding to the range  $2.5\text{--}5\text{ km s}^{-1}$ ).

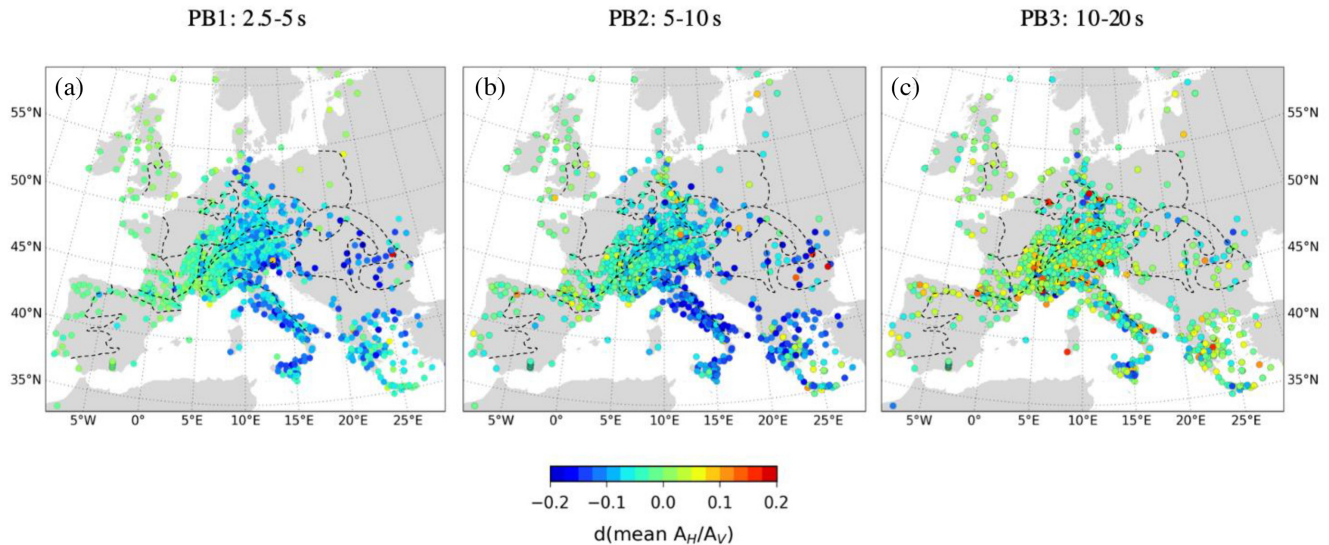


**Figure 12.** Spatial distribution of the difference between the average  $A_H/A_V$  in the summer and winter seasons in three period bands 2.5–5, 5–10 and 10–20 s. The black dashed lines in each subplot correspond to the geological boundaries shown in Fig. 1.

single station measurements. The measurement stability comes at the price of missing distributed sources (e.g. Takagi *et al.* 2018) and simultaneous multiple sources, which are better characterized with beamforming (e.g. Juretzek & Hadziioannou 2016).

In agreement with many previous studies, we observe seismic noise from source areas in the North Atlantic Ocean. We also observe significant contributions from the eastern Mediterranean Sea. The relative contribution of each source area varies with frequency, over space and time. Waves within PB3 (10–20 s period) show the simplest patterns, with the wavefield being dominated by noise sources in the North Atlantic Ocean. In PB1 (2.5–5 s) and PB2 (5–10 s), the eastern part of the Mediterranean Sea contributes significantly to the noise field. Over the year, the Significant Wave Height is not higher in the eastern Mediterranean Sea than in the western Mediterranean Sea (Cavaleri *et al.* 1991; Lionello & Sanna 2005) even though the summer seasonal mean in the eastern Mediterranean Sea may be higher than that of the western Mediterranean Sea (Chronis *et al.* 2011). As demonstrated by modelling (see e.g. Gualtieri *et al.* 2013; Gualtieri *et al.* 2019), the generation of seismic noise is strongly dependent on bathymetry, which is both significantly deeper and more irregular in the eastern part of the Mediterranean Sea as compared to the western part (e.g. Brosolo *et al.* 2012). We therefore speculate that the difference in bathymetry may be a major contributing factor to the dominance of the eastern Mediterranean Sea as a source area for seismic noise in Europe.

We observe that the Secondary microseismic peak is at significantly shorter period for the East Mediterranean Sources than for the North Atlantic Sources, possibly bringing the Primary microseismic peak of the East Mediterranean Sources into the period range 5–10 s. In that case our observed  $T_P$  (between 10 and 20 s period) has to originate from source areas in the North Atlantic. The Primary microseismic peak from the eastern Mediterranean Sea would then be embedded within the broad spectrum of PB2 (5 to 10 s period, see also end of Section 2 and Fig. S1, Supporting Information).

The source interaction underlies several of the observed parameters. The periods of the Primary ( $T_P$ ) and Secondary ( $T_S$ ) microseismic peaks are particularly sensitive indicators of the interaction of waves from the two sources. Observations such as  $T_P$  and  $T_S$ ,

and the ratio between the two, are however only proxies for the characteristics of the spectrum, as they are the results of the sum of broad spectra generated in the different source areas.

We additionally confirm that the dominant noise field in Europe has characteristics that are present only in non-diffuse wavefields. In particular, the observation of geographically coherent pattern of Rayleigh wave polarization directions, the approximately  $90^\circ$  shift between the Rayleigh propagation and the direction of highest horizontal amplitude, and the changes of these directions when the waves enter strongly heterogeneous areas such as the Alps indicate that Rayleigh and Love waves can be identified in the wavefield (see also Juretzek & Hadziioannou 2016). In the major sedimentary basins, we only have a very small number of seismic stations with reliable observations. These observations lead us to tentatively suggest that the propagation direction corresponds to trapped waves propagating between the basin edges rather than to the wave field becoming more diffuse, but more data are needed to support this hypothesis.

Our observations show that the dominance of Love over Rayleigh waves, previously obtained in a few points across Europe (Friedrich *et al.* 1998; Tanimoto *et al.* 2015; Juretzek & Hadziioannou 2016; Tanimoto *et al.* 2016), is a general observation at European scale for periods larger than 5 s. The Love to Rayleigh wave horizontal amplitude ratio in Europe increases with period, as observed also in other locations (e.g. Nishida *et al.* 2008; Gal *et al.* 2018). The amplitude ratio has no spatial pattern, and is neither altered in the Alps (which has significant surface and Moho topography), nor in the sedimentary basins. This means that the higher amplitude of the Love waves, at least in PB2 and PB3, is a characteristic of the incoming wavefield, and not the result of local scattering and wave conversion. If the Love waves were created by diffraction and scattering along the propagation path between source and receivers, we would expect the  $A_L/A_R$  ratio to decrease with period, which is the opposite of what we observe. We also observe that Rayleigh and Love waves are incoming from the same directions, in overall agreement with previous studies for the area (e.g. Friedrich *et al.* 1998; Juretzek & Hadziioannou 2016), even though we cannot exclude that the source areas differ for the two wave types. Overall,

our  $A_L/A_R$  ratios combined with the geographical stability of propagation directions, favour models where Love waves are created by ocean wave interaction combined with underlying heterogeneous structure, such as bathymetry (e.g. Nishida *et al.* 2008; Saito 2010) and/or sedimentary basins. Le Pape *et al.* (2021) provide evidence, through full waveform simulations in complex 3-D models, that this type of effect can create high amplitude Love waves, at least in the Secondary microseismic band.

Tanimoto *et al.* (2006) previously suggested that seasonal variations in H/V ratios in California could be explained by variations in the relative contributions of fundamental and higher mode Love and Rayleigh waves. Our observed variations of  $A_H/A_V$  (ratio of horizontal to vertical amplitudes) in PB2 and the comparison with a new parameter, the Beampower ratio, offer an alternative explanation: we suggest that the seasonal variations in  $A_H/A_V$  are the result of the relative influence of surface waves from nearby noise sources with that of  $P$  waves from storm areas in the Southern Hemisphere. Our interpretation is coherent with results of Takagi *et al.* (2018) who observe that the relative contribution of  $P$ -wave energy in seismic noise in Japan increases when the adjacent seas are calm. It could also explain the seasonal variations in apparent Rayleigh to Love energy ratios as observed by Tanimoto *et al.* (2016), as their results were obtained under the assumption that the  $P$ -wave energy was negligible. In any case, caution should be taken before interpreting seasonal variations of H/V of seismic noise as seasonal variations of Earth structure, for example due to water loading. The multiple contributions to the wavefield (Rayleigh, Love and  $P$  waves) also means that it will be difficult to establish meaningful H/V ratios in Europe from seismic noise only, as observed by Workman *et al.* (2017) for USArray.

It is possible to model observed noise spectra (Ardhuin *et al.* 2015; Gualtieri *et al.* 2019), but the simultaneous presence of waves from different local and global source areas as well as wave attenuation and scattering will need to be taken into account. While the scattering, in particular beneath the Alps, is stronger at short periods (as seen by the diversity of dominating propagation directions within the Alps), it remains strong also at long periods, most likely due to the depth extension of the crustal heterogeneities (80 km) beneath the Alps (Zhao *et al.* 2015). The data set at hand, which includes the AlpArray temporary experiment, would be excellent to test approaches on how to simultaneously invert for multiple seismic noise sources whilst taking into account wave propagation effects.

Observations such as these may help to build effective strategies for noise correlations. We suggest in particular exploring the following strategies:

- (i) Estimate convergence rates as a function of wave type, frequency and geographical location.
- (ii) Explore deviations from great circle propagation and rotate the noise correlations adequately to separate Rayleigh and Love waves (or detect when this separation is not possible).
- (iii) Explore whether a different weighting when stacking noise correlations over time would improve convergence. For example, one could give additional weight to time windows where the noise field is different from the yearly (or seasonal) average.
- (iv) Test the influence of weighting schemes based on  $A_H/A_V$  for the convergence of different types of waves within the noise correlations, and in particular on the convergence on the teleseismic body waves.
- (v) Dedicate additional effort to understand the link between contributing noise sources to the teleseismic body waves in the noise correlations (see e.g. Li *et al.* 2020, and Retailleau *et al.* 2020). The

paradigm of noise correlations for teleseismic body waves could change: the data interpretation could rely on the knowledge of the wavefield or, alternatively, stack only time windows with sources in areas that are optimal for a given station geometry.

## ACKNOWLEDGEMENTS

We gratefully thank the operators of the European permanent and temporary seismic networks who make their data available through EIDA (<http://www.orfeus-eu.org/eida>). The Z3 network is operated by the AlpArray Seismic Network Team: György Hetényi, Rafael Abreu, Ivo Allegretti, Maria-Theresia Apoloner, Coralie Aubert, Maxime Bes De Berc, Götz Bokelmann, Didier Brunel, Marco Capello, Martina Cărman, Adriano Cavaliere, Jérôme Ch`eze, Claudio Chiarabba, John Clinton, Glenn Cougoulat, Wayne Crawford, Luigia Cristiano, Tibor Czifra, Ezio D'Alema, Stefania Danesi, Romuald Daniel, Iva Dasović, Anne Deschamps, Jean-Xavier Dessa, Cécile Doubre, Sven Egdorf, ETHZ-SED Electronics Lab, Tomislav Fiket, Kasper Fischer, Wolfgang Friederich, Florian Fuchs, Sigward Funke, Domenico Giardini, Aladino Govoni, Zoltán Grácz, Gidera Gröschl, Stefan Heimers, Ben Heit, Davorka Herak, Marijan Herak, Johann Huber, Dejan Jarić, Petr Jedlička, Yan Jia, Hélène Jund, Edi Kissling, Stefan Klingen, Bernhard Klotz, Petr Kolínský, Michael Korn, Josef Kotek, Lothar Kühne, Krešo Kuk, Jürgen Loos, Deny Malengros, Lucia Margheriti, Christophe Maron, Xavier Martin, Marco Massa, Francesco Mazzarini, Thomas Meier, Laurent Métral, Irene Molinari, Milena Moretti, Helena Munzarová, Anna Nardi, Jurij Pahor, Anne Paul, Catherine Péquegnat, Damiano Pesaresi, Davide Piccinini, Claudia Piromallo, Thomas Plenefisch, Jaroslava Plomerová, Silvia Pondrelli, Snježan Prevolnik, Roman Racine, Marc Régnier, Miriam Reiss, Joachim Ritter, Georg Rumpker, Simone Salimbeni, Detlef Schulte-Kortnack, Werner Scherer, Sven Schippkus, Vesna Šipka, Daniele Spallarossa, Kathrin Spieker, Josip Stipčević, Angelo Strollo, Bálint Süle, Gyöngyvér Szanyi, Eszter Szücs, Christine Thomas, Frederik Tilmann, Stefan Ueding, Massimiliano Vallocchia, Luděk Vecsey, René Voigt, Joachim Wassermann, Zoltán Wéber, Christian Weidle, Viktor Westergom, Gauthier Weyland, Stefan Wiemer, David Wolyniec, Thomas Zieke and Mladen Živčić. All data processing is carried out with python software, and the community software Obspy (Krischer *et al.* 2015) is used for the data processing. We thank P. Boué and A. Paul for initial comments to the manuscript. This work received support from the Seismology and Earthquake Engineering Research Infrastructure Alliance for Europe (SERA) project, funded under the European Union's Horizon 2020 research and innovation program under grant agreement number 730900. During this work, the first author was also supported by the postdoc scholarship provided by Prof. Ben-Zion at University of Southern California. ISTERre is part of Labex OSUG@2020 (ANR10 LABX56). We thank K. Nishida and an anonymous reviewer for thoughtful and constructive reviews.

## 5 DATA AVAILABILITY

We analysed seismic broad-band stations (three components) within latitudes 30°N–65°N and longitudes 10°W–30°E, for one decade of data (2011–2019), and for which data are distributed by the ORFEUS service European Integrated Data Archive, EIDA (Strollo *et al.* 2021). We also included a presently embargoed data set, AlpArray (AlpArray seismic network 2015).

*Waveform* data used in this paper belong to the permanent networks with codes: AC (Institute of Geosciences, Energy, Water and Environment (IGEWE), Albania 2002), BE (Belgium, R.O.O. (Royal Observatory of Belgium) 1985), BS (National Institute of Geophysics, G., Bulgaria 1980), BW (Department of Earth and Environmental Sciences, Geophysical Observatory, University of Munchen 2001), C4 (CERN, ETH Zurich 2016), CA (Institut Cartogràfic i Geològic de Catalunya 1984), CH (Swiss Seismological Service (SED) At ETH Zurich 1983), CL (Corinth Rift Laboratory Team And RESIF Datacenter 2013), CR (University of Zagreb 2001), CZ (Institute of Geophysics, A.O.S.O.T.C.R. (Academy of Sciences of the Czech Republic) 1973), DK (GEUS Geological Survey of Denmark and Greenland 1976), EE (Geological Survey of Estonia (GSE) 1998), EI (INSN (Irish National Seismic Network) 1993), FR (RESIF (Réseau sismologique et géodésique français) 1995), G (Institut De Physique Du Globe De Paris (IPGP), & Ecole Et Observatoire Des Sciences De La Terre De Strasbourg (EOST) 1982), GB (British Geological Survey 1970), GE (GE-OFON Data Centre 1993), GR (Federal Institute for Geosciences and Natural Resources (BGR) 1976), GU (University of Genova 1967), HC (Technological Educational Institute of Crete 2006), HE (Institute Of Seismology, U.O.H. (University of Helsinki) 1980), HL (National Observatory of Athens, I.O.G. (Institute of Geodynamics) 1997), HP (University of Patras, G.D. 2000), HT (Aristotle University Of Thessaloniki Seismological Network 1981), HU (Kövesligethy Radó Seismological Observatory (Geodetic And Geophysical Research Institute, Research Centre For Astronomy And Earth Sciences, Hungarian Academy Of Sciences (MTA CSFK GGI KRSZO) 1992), IB (Institute Earth Sciences ‘Jaume Almera’ CSIC (ICTJA Spain) 2007), IU (Albuquerque Seismological Laboratory (ASL)/USGS 1988), IV (INGV Seismological Data Centre 2006), KO (Bogazici University Kandilli Observatory And Earthquake Research Institute 2001), LC (Laboratorio Subteraneo De Canfranc 2011), LX (Instituto Dom Luiz (IDL) – Faculdade De Ciências Da Universidade De Lisboa 2003), MD (Geological And Seismological Institute Of Moldova 2007), ME (Sector for Seismology, I.O.H. (Institute of Hydrometeorology and Seismology of Montenegro) 1982), MN (MedNet Project Partner Institutions 1990), MT (French Landslide Observatory – Seismological Datacenter/RESIF 2006), NI (OGS (Istituto Nazionale Di Oceanografia E Di Geofisica Sperimentale) And University Of Trieste 2002), NL (KNMI (Royal Netherlands Meteorological Institute) 1993), NS (University of Bergen 1982), OE (ZAMG – Zentralanstalt Für Meteorologie Und Geodynamik 1987), OT (University of Bari ‘Aldo Moro’ 2013), OX (OGS (Istituto Nazionale Di Oceanografia E Di Geofisica Sperimentale) 2016), PL (Polish Academy of Sciences (PAN) Polskiej Akademii Nauk 1990), PM (Instituto Português Do Mar E Da Atmosfera, I.P. 2006), RF (University Of Trieste 1993), RO (National Institute For Earth Physics (NIEP Romania) 1994), SI (ZAMG – Central Institute for Meteorology and Geodynamics 2006), SK (ESI SAS (Earth Science Institute Of The Slovak Academy Of Sciences) 2004), ST (Geological Survey-Provincia Autonoma Di Trento 1981), SX (Leipzig University 2001), TH (Jena, F.S.U. (Friedrich-Schiller-Universitaet) 2009), TT (Institut National de la Météorologie, Tunis 2008), TV (Istituto Nazionale di Geofisica e Vulcanologia (INGV) 2008), UK (University of Leicester (SEIS UK) 2005), WM (San Fernando Royal Naval Observatory (ROA), Universidad Complutense De Madrid (UCM), Helmholtz-Zentrum Potsdam Deutsches GeoForschungsZentrum (GFZ), Universidade De Evora (UEVORA, Portugal), & Institute Scientifique Of RABAT (ISRABAT, Morocco) 1996). Single Station COI (Coimbra, Portugal) was also used.

We also used data of temporary experiments, namely AlpArray [network code Z3 (2015–2020), Hetényi *et al.* (2018)], CICALPS [network code YP (2012–2013), Zhao *et al.* (2016)], HIRE [network code 9C (2010–2011), Heit *et al.* (2010)], Pollino Seismic Experiment [network code 4A (2012–2014), Passarelli *et al.* (2012)], PYROPE [network code X7 (2010–2014), Chevrot *et al.* (2017)] and WILAS [network code 8A (2010–2012), Dias *et al.* (2010)].

## REFERENCES

- Albuquerque Seismological Laboratory (ASL)/USGS, 1988. *Global Seismograph Network (GSN–IRIS/USGS)*, International Federation of Digital Seismograph Networks, doi:10.7914/SN/IU.
- Alder, C., Debayle, E., Bodin, Th., Paul, A., Stehly, L. & Pedersen, H.A., AlpArray Working Group, Evidence for radial anisotropy in the lower crust of the Apennines from Bayesian ambient noise tomography in Europe. 2021. *Geophys. J. Int.*, **226**(2), 941–967.
- AlpArray Seismic Network, 2015. *AlpArray Seismic Network (AASN) temporary component*, AlpArray Working Group, doi:10.12686/alparray/z3.2015.
- Ardhuin, F., Gualtieri, L. & Stutzmann, E., 2015. How ocean waves rock the Earth: two mechanisms explain microseisms with periods 3 to 300 s, *Geophys. Res. Lett.*, **42**, 765–772.
- Ardhuin, 2018. Large-scale forces under surface gravity waves at a wavy bottom: a mechanism for the generation of primary microseisms, *Geophys. Res. Lett.*, **45**(16), 8173–8181.
- Aristotle University Of Thessaloniki Seismological Network, 1981. *Permanent Regional Seismological Network operated by the Aristotle University of Thessaloniki*, International Federation of Digital Seismograph Networks, doi:10.7914/SN/HT.
- Belgium, R.O.O., 1985. *Belgian Seismic Network*, International Federation of Digital Seismograph Network, doi:10.7914/SN/BE.
- Beucler, E., Mocquet, A., Schimmel, M., Chevrot, S., Quillard, O., Vergne, J. & Sylvander, M., 2014. Observation of deep water microseisms in the North Atlantic Ocean using tide modulations, *Geophys. Res. Lett.*, **42**(2), 316–322.
- Bogazici University Kandilli Observatory & Earthquake Research Institute, 2001. *Bogazici University Kandilli Observatory And Earthquake Research Institute*, International Federation of Digital Seismograph Networks, doi:10.7914/SN/KO.
- Boué, P., Poli, P., Campillo, M., Pedersen, H.A., Briand, X. & Roux, P., 2013. Teleseismic correlations of ambient seismic noise for deep global imaging of the Earth, *Geophys. J. Int.*, **194**(2), 844–848.
- Boué, P., Poli, P., Campillo, M. & Roux, P., 2014. Reverberations, coda waves and ambient noise: correlations at the global scale and retrieval of the deep phases, *Earth planet. Sci. Lett.*, **391**, 137–145.
- Brenguier, F., Campillo, M., Hadziioannou, C., Shapiro, N.M., Nadeau, R.M. & Larose, E., 2008. Postseismic relaxation along the San Andreas fault at Parkfield from continuous seismological observations, *Science*, **321**(5895), 1478–1481.
- Brenguier, F. *et al.*, 2012. First results from the UnderVolc high resolution seismic and GPS network deployed on Piton de la Fournaise Volcano, *Seismol. Res. Lett.*, **83**(1), 97–102.
- British Geological Survey, 1970. Great Britain Seismograph Network.
- Bromirski, P.D., Duennebieber, F.K. & Stephen, R.A., 2005. Mid-ocean microseisms, *Geochem. Geophys. Geosyst.*, **6**(4), Q04009, doi:10.1029/2004GC000768.
- Brosolo, L., Mascle, J. & Loubrieu, B., 2012. *Morphobathymetric Map of the Mediterranean Sea*, publication CCGM/CGMW, UNESCO, Paris, © CCGM-CGMW 2012 - ISBN 978-2-917310-12-0.
- Cavaleri, L., Bertotti, L. & Lionello, P., 1991. Wind wave cast in the Mediterranean Sea, *J. geophys. Res. – Oceans*, **96**(C6), 10739–10762.
- CERN, 2016. *CERN Seismic Network. ETH Zurich, Other/Seismic Network*, doi:10.12686/sed/networks/c4.
- Cessaro, R.K., 1994. Sources of Primary and Secondary Microseisms, *Bull. seism. Soc. Am.*, **84**(1), 142–148.

- Chevrot, S. & Sylvander, M., RESIF, 2017. *Seismic network X7: PYROPE PYRenean Observational Portable Experiment (RESIF-SISMOB)*, RESIF – Réseau Sismologique et géodésique Français, doi:10.15778/resif.x72010.
- Chevrot, S., Sylvander, M., Benahmed, S., Ponsolles, C., Lefèvre, J.M. & Paradis, D., 2007. Source locations of secondary microseisms in western Europe: evidence for both coastal and pelagic sources, *J. geophys. Res.*, **112**, B11301, doi:10.1029/2007JB005059.
- Chronis, T., Papadopoulos, V. & Nikolopoulos, E.I., 2011. QuickSCAT observations of extreme wind events over the Mediterranean and Black Seas during 2000–2008, *Int. J. Climat.*, **31**(14), 2068–2077.
- Colombi, A., Chaput, J., Brenguier, F., Hillers, G., Roux, P. & Campillo, M., 2014. On the temporal stability of the coda of ambient noise correlations, *C. R. Geosci.*, **346**(2014), 307–316.
- Corinth Rift Laboratory Team & RESIF Datacenter, 2013. *CL – Corinth Rift Laboratory Seismological Network (CRLNET)*. RESIF – Réseau Sismologique et géodésique Français, doi:10.15778/RESIF.CL.
- Cotte, N., Pedersen, H.A., Campillo, M., Farra, V. & Cansi, Y., 2000. Off-great circle propagation of intermediate period surface waves as observed on a dense array in the French Alps, *Geophys. J. Int.*, **142**(3), 825–840.
- Craig, D., Bean, C.J., Lokmer, I. & Möllhoff, M., 2016. Correlation of wavefield-separated ocean-generated microseisms with North Atlantic Source Regions, *Bull. seism. Soc. Am.*, **106**(3), 1002–1010.
- Crotwell, H.P., Owens, T.J. & Ritsema, J., 1999. The TauP Toolkit: flexible seismic travel-time and ray-path utilities, *Seismol. Res. Lett.*, **70**(2), 154–160.
- Department of Earth and Environmental Sciences, Geophysical Observatory, University of Munchen, 2001. BayernNetz [Data set]. International Federation of Digital Seismograph Networks, doi:10.7914/SN/BW.
- Dias, N.A., Silveira, G. & Haberland, C.(2010). Data of the temporary seismic WILAS network. *GFZ Data Services*, doi:10.14470/3N7565750319.
- ESI SAS (Earth Science Institute Of The Slovak Academy Of Sciences), 2004. National Network of Seismic Stations of Slovakia. *Deutsches Geoforschungszentrum GFZ*, doi:10.14470/FX099882.
- Essen, H.-H., Krüger, F., Dahm, T. & Grevemeyer, I., 2003. On the generation of secondary microseisms observed in northern and central Europe, *J. geophys. Res.*, **108**(B10), 2506. doi:10.1029/2002JB002338.
- Evangelidis, C.P. & Melis, N.S., 2012. Ambient noise levels in Greece as recorded at the Hellenic Unified Seismic Network, *Bull. seism. Soc. Am.*, **102**(6), 2507–2517.
- Fan, Y. & Snieder, R., 2009. Required source distribution for interferometry of waves and diffusive fields, *Geophys. J. Int.*, **179**(2), 1232–1244.
- Federal Institute for Geosciences and Natural Resources (BGR), 1976. *German Regional Seismic Network (GRSN)*, Federal Institute for Geosciences and Natural Resources (BGR), doi:10.25928/mbx6-hr74.
- Ferretti, G., Zunino, A., Scafidi, D., Barani, S. & Spallarossa, D., 2013. On microseisms recorded near the Ligurian coast (Italy) and their relationship with sea wave height, *Geophys. J. Int.*, **194**(2013), 524–533.
- Flinn, E.A., 1965. Signal analysis using rectilinearity and direction of particle motion, *Proc. IEEE*, **53**(12), 1874–1876.
- French Landslide Observatory – Seismological Datacenter /RESIF, 2006. *Observatoire Multi-disciplinaire des Instabilités de Versants (OMIV)*, RESIF – Réseau Sismologique et géodésique Français, doi:10.15778/RESIF.MT.
- Friedrich, A., Krüger, F. & Klinge, K., 1998. Ocean-generated microseismic noise located with the Gräfenberg array, *J. Seism.*, **2**, 47–64.
- Froment, B., Campillo, M., Roux, P., Gouédard, P., Verdel, A. & Weaver, R.L., 2010. Estimation of the effect of nonisotropically distributed energy on the apparent arrival time in correlations, *Geophysics*, **75**(5), SA85–SA93.
- Fukao, Y., Nishida, K. & Kobayashi, N.(2010). Seafloor topography, ocean infragravity waves, and background Love and Rayleigh waves, *J. geophys. Res. Solid Earth*, **115**(B4), B04302, doi:10.1029/2009JB006678.
- Gal, M., Reading, A.M., Ellingsen, S.P., Koper, K.D. & Burlacu, R., 2017. Full wavefield decomposition of high-frequency secondary microseisms reveals distinct arrival azimuths for Rayleigh and Love waves, *J. geophys. Res. Solid Earth*, **122**, 4660–4675.
- Gal, M., Reading, A.M., Rawlinson, N. & Schulte-Pelkum, V., 2018. Matched field processing of three-component seismic array data applied to Rayleigh and Love microseisms. *J. geophys. Res.: Solid Earth*, **123**, 6871–6889.
- GEOFON Data Centre, 1993. GEOFON Seismic Network. *Deutsches Geoforschungszentrum GFZ*, doi:10.14470/TR560404.
- Geological And Seismological Institute Of Moldova, 2007. *Moldova Digital Seismic Network*, International Federation of Digital Seismograph Networks, doi:10.7914/SN/MD.
- Geological Survey of Estonia (GSE), 1998. Estonian Seismic Network.
- Geological Survey-Provincia Autonoma Di Trento, 1981. *Trentino Seismic Network*, International Federation of Digital Seismograph Network, doi:10.7914/SN/ST.
- Gerstoft, P., Shearer, P.M., Harmon, N. & Zhang, J., 2008. Global P, PP, and PKP wave microseisms observed from distant storms, *Geophys. Res. Lett.*, **35**, L23306, doi:10.1029/2008GL036111.
- GEUS Geological Survey of Denmark and Greenland, 1976. Danish Seismological Network.
- Gualtieri, L., Stutzmann, E., Capdeville, Y., Arduin, F., Schimmel, M., Mangeney, A. & Morelli, A., 2013. Modelling secondary microseismic noise by normal mode summation, *Geophys. J. Int.*, **193**(3), 1732–1745.
- Gualtieri, L., Stutzmann, E., Capdeville, Y., Farra, V., Mangeney, A. & Morelli, A., 2015. On the shaping factors of the secondary microseismic wavefield, *J. geophys. Res. Solid Earth*, **120**, 6241–6262.
- Gualtieri, L., Stutzmann, E., Juretzek, C., Hadziioannou, C. & Arduin, F., 2019. Global scale analysis and modelling of primary microseisms, *Geophys. J. Int.*, **218**, 560–572.
- Gutenberg, B., 1912 “Die seismische Bodenunruhe,” (Dissertation, Göttingen), *Getlands Beiträge zur Geophysik*, **11**, 314–353.
- Gutenberg, B., 1921 “Untersuchungen über die Bodenunruhe mit Perioden von 4–10 Sekunden in Europa,” *Vergöfentlichungen des Zentralbureaus der Internationalen Seismologischen Assoziation*, Strassburg.
- Gutenberg, B., 1931. Microseisms in North America, *Bull. seism. Soc. Am.*, **21**(1), 1–24.
- Handy, M.R., Schmid, S., Bousquet, R., Kissling, E. & Bernoulli, D., 2010. Reconciling plate-tectonic reconstructions of Alpine Tethys with the geological-geophysical record of spreading and subduction in the Alps, *Earth-Sci. Rev.*, **102**(3-4), 121–158.
- Hasselmann, K., 1963. A statistical analysis of the generation of microseisms, *Rev. Geophys.*, **1**(2), 177–210.
- Haubrich, R.A. & McCamy, K., 1969. Microseisms: coastal and Pelagic Sources, *Rev. Geophys.*, **7**(3), 539–571.
- Heit, B., Yuan, X. & Mancilla, F.D.L., 2010. High Resolution Seismological Profiling across Sierra Nevada (HIRE). *Deutsches Geoforschungszentrum GFZ*, doi:10.14470/4P7565788335.
- Hobiger, M., Biham, N.L., Cornou, C. & Bard, P.-Y., 2009. Rayleigh wave ellipticity estimation from ambient seismic noise using single and multiple vector-sensor techniques, 17<sup>th</sup> European Signal Processing Conference (EUSIPCO 2009), pp.2037–2041, IEEE.
- INGV Seismological Data Centre, 2006. *Rete Sismica Nazionale (RSN)*, Istituto Nazionale di Geofisica e Vulcanologia (INGV), Italy, doi:10.13127/SD/X0FXnH7QfY.
- INSN, 1993. *Irish National Seismic Network, operated by the Dublin Institute for Advanced Studies and supported by the Geological Survey Ireland*, International Federation of Digital Seismograph Networks, doi:10.7914/SN/EI.
- Institut Cartogràfic I Geològic De Catalunya, 1984. *Catalan Seismic Network [Data set]*, International Federation of Digital Seismograph Networks, doi:10.7914/SN/CA.
- Institut De Physique Du Globe De Paris (IPGP) & Ecole Et Observatoire Des Sciences De La Terre De Strasbourg (EOST), 1982. *GEOSCOPE, French Global Network of Broad band Seismic Stations*, Institut de Physique du Globe de Paris (IPGP), doi:10.18715/GEOSCOPE.G.
- Institut National de la Météorologie, Tunis, 2008. Seismic Network of Tunisia.
- Istituto Nazionale di Geofisica e Vulcanologia (INGV), 2008. INGV Experiments Network.

- Institute Earth Sciences “Jaume Almera” CSIC (ICTJA Spain), 2007. *IberArray*, International Federation of Digital Seismograph Networks, doi:10.7914/SN/IB.
- Institute of Geophysics, A.O.S.O.T.C.R., 1973. *Czech Regional Seismic Network*, International Federation of Digital Seismograph Networks, doi:10.7914/SN/CZ.
- Institute of Geosciences, Energy, Water and Environment (IGEWE), Albania, 2002. *Albanian Seismological Network*, International Federation of Digital Seismograph Networks, doi:10.7914/SN/AC.
- Institute Of Seismology, U.O.H., 1980. *The Finnish National Seismic Network. GFZ Data Services*, Other/Seismic Network, doi:10.14470/UR044600.
- Instituto Dom Luiz (IDL) – Faculdade De Ciências Da Universidade De Lisboa, 2003. *University of Lisbon Seismic Network*, International Federation of Digital Seismograph Networks, doi:10.7914/SN/LX.
- Instituto Português Do Mar E Da Atmosfera, I.P., 2006. *Portuguese National Seismic Network [Data set]*, International Federation of Digital Seismograph Networks, doi:10.7914/SN/PM.
- Jena, F.S.U., 2009. *Thüringer Seismologisches Netz (TSN)*, International Federation of Digital Seismograph Networks, doi:10.7914/SN/TH.
- Juretzek, C. & Hadziioannou, C., 2016. Where do ocean microseisms come from? a study of Love-to-Rayleigh wave ratios, *J. geophys. Res. Solid Earth*, **121**, 6741–6756.
- Juretzek, C. & Hadziioannou, C., 2017. Linking source region and ocean wave parameters with the observed primary microseismic noise, *Geophys. J. Int.*, **211**(3), 1640–1654.
- Kästle, E.D., El-Sharkawy, A., Boschi, L., Meier, T., Rosenberg, C., Bellahsen, N., Cristiano, L. & Weidle, C., 2018. Surface-wave tomography of the European Alps using Ambient-Noise and Earthquake phase-velocity measurements, *J. geophys. Res. (Solid Earth)*, **123**(2), 1770–1792.
- Kedar, S., Longuet-Higgins, M., Webb, F., Graham, N., Clayton, R. & Jones, C., 2008. The origin of deep ocean microseisms in the North Atlantic Ocean, *Proc. R. Soc. A*, **464**(2091), 777–793.
- Kennett, B.L.N. & Engdahl, E.R., 1991. Travel times for global earthquake location and phase association, *Geophys. J. Int.*, **105**, 429–465.
- Kimman, W.P., Campman, X. & Trampert, J., 2012. Characteristics of seismic noise: fundamental and higher mode energy observed in the northeast of the Netherlands, *Bull. seism. Soc. Am.*, **102**(4), 1388–1399.
- Klotz, O., 1908. Microseisms, *J. R. Astron. Soc. Can.*, **2**, 195.
- KNMI, 1993. *Netherlands Seismic and Acoustic Network. Royal Netherlands Meteorological Institute (KNMI)*, Other/Seismic Network, doi:10.21944/e970fd34-23b9-3411-b366-e4f72877d2e5.
- Koper, K.D., Seats, K. & Benz, H., 2010. On the composition of Earth’s short-period seismic noise field, *Bull. seism. Soc. Am.*, **100**(2), 606–617.
- Koper, K. & Burlacu, R., 2015. The fine structure of double-frequency microseisms recorded by seismometers in North America, *J. geophys. Res.: Solid Earth*, **120**(3), 1677–1691.
- Kövesligethy Radó Seismological Observatory (Geodetic And Geophysical Research Institute, Research Centre For Astronomy And Earth Sciences, Hungarian Academy Of Sciences (MTA CSFK GGI KRSZO), 1992. *Hungarian National Seismological Network. Deutsches GeoForschungsZentrum GFZ*, doi:10.14470/UH028726.
- Krischer, L., Megies, T., Barsch, R., Beyreuther, M., Lecocq, T., Caudron, C. & Wassermann, J., 2015. ObsPy: a bridge for seismology into the scientific Python ecosystem, *Comput. Sci. Discov.*, **8**, 014003, doi:10.1088/1749-4699/8/1/014003.
- Laboratorio Subterraneo De Canfranc, 2011. *LSC (Laboratorio Subterraneo Canfranc)*, International Federation of Digital Seismograph Networks, doi:10.7914/SN/LC.
- Landès, M., Hubans, F., Shapiro, N.M., Paul, A. & Campillo, M., 2010. Origin of deep ocean microseisms by using teleseismic body waves, *J. geophys. Res.*, **115**, B05302, doi:10.1029/2009JB006918.
- Le Pape, F., Craig, D. & Bean, C.J., 2021. How deep ocean-land coupling controls the generation of secondary microseism Love waves, *Nat. Comm.*, **12**, 2332, doi:10.1038/s41467-021-22591-5.
- Lecocq, T., Longuevergne, L., Pedersen, H.A., Brenguier, F. & Stammler, K., 2017. Monitoring ground water storage at mesoscale using seismic noise: 30 years of continuous observation and thermo-elastic and hydrological modelling, *Sci. Rep.*, **7**, 14241, <https://doi.org/10.1038/s41598-017-14468-9>.
- Leipzig University, 2001. *SXNET Saxon Seismic Network*, International Federation of Digital Seismograph Networks, doi:10.7914/SN/SX.
- Lepore, S. & Grad, M., 2018. Analysis of the primary and secondary microseisms in the wavefield of the ambient noise recorded in northern Poland, *Acta Geophys.*, **66**, 915–929.
- Li, L., Boué, P., Retailleau, L. & Campillo, M., 2020. Spatiotemporal correlation analysis of noise-derived seismic body waves with ocean wave climate and microseism sources, *Geochem. Geophys. Geosyst.*, **21**, e2020GC009112, doi:10.1029/2020GC009112.
- Lionello, P. & Sanna, A., 2005. Mediterranean wave climate variability and its links with NAO and Indian Monsoon, *Clim. Dyn.*, **25**(6), 611–623.
- Liu, Q. et al., 2016. Source locations of teleseismic P, SV, and SH waves observed in microseisms recorded by a large aperture seismic array in China, *Earth planet. Sci. Lett.*, **449**, 39–47.
- Longuet-Higgins, M.S., 1950. A theory of the origin of microseisms, *Philos. Trans. R. Soc. Lond.*, **243**(857), 1–35.
- Lu, Y., Stehly, L. & Paul, A., AlpArray Working Group, 2018. High-resolution surface wave tomography of the European crust and uppermost mantle from ambient seismic noise, *Geophys. J. Int.*, **214**(2), 1136–1150.
- Lu, Y., Stehly, L., Brossier, R. & Paul, A., AlpArray Working Group, 2020. Imaging Alpine crust using ambient noise wave-equation tomography, *Geophys. J. Int.*, **222**(1), 69–85.
- Marzorati, S. & Bindi, D., 2006. Ambient noise levels in north central Italy, *Geochem. Geophys. Geosyst.*, **7**(9), Q09010, doi:10.1029/2006GC001256.
- Marzorati, S. & Bindi, D., 2008. Characteristics of ambient noise cross correlations in northern Italy within the frequency range of 0.1–0.6 Hz, *Bull. seism. Soc. Am.*, **98**(3), 1389–1398.
- MedNet Project Partner Institutions, 1990. *Mediterranean Very Broadband Seismographic Network (MedNet)*, Istituto Nazionale di Geofisica e Vulcanologia (INGV), <https://doi.org/10.13127/SD/fBBBtdtd6q>.
- Meier, U., Shapiro, N.M. & Brenguier, F., 2010. Detecting seasonal variations in seismic velocities within Los Angeles basin from correlations of ambient seismic noise, *Geophys. J. Int.*, **181**, 985–996.
- Milne, J. 1886. *Earthquakes and other Movements*, K. Paul Trench, London, 343pp.
- Moni, A., Craig, D. & Bean, C.J., 2013. Separation and location of microseism sources, *Geophys. Res. Lett.*, **40**, 3118–3122.
- Nakamura, Y., 1989. A method for dynamic characteristics estimation of subsurface using microtremor on the ground surface, *QR Railway Tech. Res. Inst.*, **30**, 25–33.
- National Institute For Earth Physics (NIEP Romania), 1994. *Romanian Seismic Network*, International Federation of Digital Seismograph Networks, doi:10.7914/SN/RO.
- National Institute Of Geophysics, G., 1980. *National Seismic Network of Bulgaria*, International Federation of Digital Seismograph Networks, doi:10.7914/SN/BS.
- National Observatory of Athens, I.O.G., 1997. *National Observatory of Athens Seismic Network*, International Federation of Digital Seismograph Networks, doi:10.7914/SN/HL.
- Neubauer, F., 2003. Geology of Europe, in De Vivo, B., Grasemann, B. & Stüwe, K., eds, *Volume Geology. Encyclopedia of Life Supporting Systems*, UNESCO Publishing-Eolss Publishers, Oxford, UK (Online version: [www.eolss.net](http://www.eolss.net)).
- Nishida, K., Kawakatsu, H., Fukao, Y. & Obara, K., 2008. Background Love and Rayleigh waves simultaneously generated at the Pacific Ocean floors, *Geophys. Res. Lett.*, **35**, L16307.
- Nishida, K. & Takagi, R., 2016. Teleseismic S wave microseisms, *Science*, **353**(6302), 919–921.
- OGS (Istituto Nazionale Di Oceanografia E Di Geofisica Sperimentale), 2016. *North-East Italy Seismic Network*, International Federation of Digital Seismograph Networks, doi:10.7914/SN/OX.
- OGS (Istituto Nazionale Di Oceanografia E Di Geofisica Sperimentale) And University Of Trieste, 2002. *North-East Italy Broadband*

- Network, International Federation of Digital Seismograph Networks, doi:10.7914/SN/NI.
- Passarelli, L. *et al.*, 2012. *Pollino Seismic Experiment (2012-2014)*, Deutsches GeoForschungsZentrum GFZ, doi:10.14470/9N904956.
- Pedersen, H.A. & Krüger, F., the SVEKALAPKO Seismic Tomography working Group, 2007. Influence of the seismic noise characteristics on noise correlations in the Baltic Shield, *Geophys. J. Int.*, **168**(1), 197–210.
- Pedersen, H.A. & Colombi, A., 2018. Body waves from a single source area observed in noise correlations at arrival times of reflections from the 410 discontinuity, *Geophys. J. Int.*, **214**(2), 1125–1135.
- Poli, P., Campillo, M. & de Hoop, M., 2017. Analysis of intermediate period correlations of coda from deep earthquakes, *Earth planet. Sci. Lett.*, **477**, 147–155.
- Polish Academy of Sciences (PAN) Polskiej Akademii Nauk, 1990, Polish Seismological Network.
- RESIF, 1995. *RESIF-RLBP French Broad-band network, RESIF-RAP strong motion network and other seismic stations in metropolitan France*, RESIF – Réseau Seismologique et géodésique Français, doi:10.15778/RESIF.FR.
- Retailleau, L., Boué, P., Stehly, L. & Campillo, M., 2017. Locating micro-seism sources using spurious arrivals in intercontinental noise correlations. *J. geophys. Res. Solid Earth*, **122**, 8107–8120.
- Retailleau, L., Boué, P., Li, L. & Campillo, M., 2020. Ambient seismic noise imaging of the lowermost mantle beneath the North Atlantic Ocean, *Geophys. J. Int.*, **222**(2), 1339–1351.
- Rost, S. & Thomas, C., 2002. Array seismology: methods and applications. *Rev. Geophys.*, **40**(3), 2–1-2-27.
- Ruigrok, E., Draganov, D. & Wapenaar, K., 2008. Global-scale seismic interferometry: theory and numerical examples, *Geophys. Prospect.*, **56**(3), 395–417.
- Sabra, K.G., Gerstoft, P., Roux, P., Kuperman, W.A. & Fehler, M.C., 2005. Surface wave tomography from microseisms in Southern California, *Geophys. Res. Lett.*, **32**(14), L14311, doi:10.1029/2005GL023155.
- Saito, T., 2010. Love-wave excitation due to the interaction between a propagating ocean wave and the sea-bottom topography, *Geophys. J. Int.*, **182**(3), 1515–1523.
- San Fernando Royal Naval Observatory (ROA), Universidad Complutense De Madrid (UCM), Helmholtz-Zentrum Potsdam Deutsches GeoForschungsZentrum (GFZ), Universidade De Evora (UEVORA, Portugal) & Institute Scientifique Of RABAT (ISRABAT, Morocco), 1996. *The Western Mediterranean BB Seismic Network*, Deutsches GeoForschungsZentrum GFZ, doi:10.14470/JZ581150.
- Schmid, S.M., Fügenschuh, B., Kissling, E. & Schuster, R., 2004. Tectonic map and overall architecture of the Alpine orogen, *Eclogae Geol. Helv.*, **97**(1), 93–117.
- Sector for Seismology, I.O.H., 1982. *Montenegrin Seismic Network*, Sector for Seismology, Institute of Hydrometeorology and Seismology of Montenegro, doi:10.7914/SN/ME.
- Sergeant, A., Stutzmann, E., Maggi, A., Schimmel, M., Arduin, F. & Obrebski, M., 2013. Frequency-dependent noise sources in the North Atlantic Ocean, *Geochem. Geophys.*, **14**(12), 5341–5353.
- Shapiro, N.M. & Campillo, M., 2004. Emergence of broadband Rayleigh waves from correlations of the ambient seismic noise, *Geophys. Res. Lett.*, **31**, L07614, doi:10.1029/2004GL019491.
- Shapiro, N.M., Campillo, M., Stehly, L. & Ritzwoller, M.H., 2005. High-resolution surface-wave tomography from ambient seismic noise, *Science*, **307**(5715), 1615–1618.
- Snieder, R., Wapenaar, K. & Larner, K., 2006. Spurious multiples in seismic interferometry of primaries, *Geophys. J. Int.*, **168**(4), S1111–S1124.
- Snieder, R. & Sens-Schönfelder, C., 2015. Seismic interferometry and stationary phase at caustics, *J. geophys. Res. Solid Earth*, **120**, 4333–4343.
- Stehly, L., Campillo, M. & Shapiro, N.M., 2006. A study of the seismic noise from its long-range correlation properties, *J. geophys. Res. Solid Earth*, **111**, B10306, doi:10.1029/2005JB004237.
- Stich, D. & Morelli, A., 2007. Reflection of seismic surface waves at the northern Apennines, *Earth planet. Sci. Lett.*, **259**(1-2), 149–158.
- Stich, D., Danecek, P., Morelli, A. & Tromp, J., 2009. Imaging lateral heterogeneity in the northern Apennines from time reversal of reflected surface waves, *Geophys. J. Int.*, **177**(2), 543–554.
- Strollo, A. *et al.*, 2021. EIDA: the European Integrated Data Archive and Service Infrastructure within ORFEUS. *Seismol. Res. Lett.*, **92**(3), 1788–1795.
- Swiss Seismological Service (SED) at ETH Zurich, 1983. *National Seismic Networks of Switzerland*, ETH Zürich, doi:10.12686/sed/networks/ch.
- Takagi, R., Nishida, K., Maeda, T. & Obara, K., 2018. Ambient seismic noise wavefield in Japan characterized by polarization analysis of Hi-net records, *Geophys. J. Int.*, **215**(3), 1682–1699.
- Tanimoto, T., Ishimaru, S. & Alvizuri, C., 2006. Seasonality in particle motion of microseisms, *Geophys. J. Int.*, **166**(1), 253–266.
- Tanimoto, T., Hadziioannou, C., Igel, H., Wasserman, J., Schreiber, U. & Gebauer, A., 2015. Estimate of Rayleigh-to-Love wave ratio in the secondary microseism by collocated ring laser and seismograph, *Geophys. Res. Lett.*, **42**(8), 2650–2655.
- Tanimoto, T., Hadziioannou, C., Igel, H., Wassermann, J., Schreiber, U., Gebauer, A. & Chow, B., 2016. Seasonal variations in the Rayleigh-to-Love wave ratio in the secondary microseism from collocated ring laser and seismograph, *J. geophys. Res. Solid Earth*, **121**(4), 2447–2459.
- Technological Educational Institute of Crete, 2006. *Seismological Network of Crete*, International Federation of Digital Seismograph Networks, doi:10.7914/SN/HC.
- University Of Bari “Aldo Moro”, 2013. *OTRIONS, Seismic Networks of Gargano Area (Italy)*, International Federation of Digital Seismograph Networks, doi:10.7914/SN/OT.
- University of Bergen, 1982. *University of Bergen Seismic Network*, International Federation of Digital Seismograph Networks, <https://doi.org/10.7914/SN/NS>.
- University Of Genova, 1967. *Regional Seismic Network of North Western Italy*, International Federation of Digital Seismograph Networks, doi:10.7914/SN/GU.
- University of Leicester (SEIS UK), 2005, UK Schools Network.
- University of Patras, G.D., 2000. *PSLNET, Permanent Seismic Network operated by the University of Patras, Greece*, International Federation of Digital Seismograph Networks, doi:10.7914/SN/HP.
- University Of Trieste, 1993. *Friuli Venezia Giulia Accelerometric Network*, International Federation of Digital Seismograph Networks, doi:10.7914/SN/RF.
- University Of Zagreb, 2001. *Croatian Seismograph Network*, International Federation of Digital Seismograph Networks, doi:10.7914/SN/CR.
- Workman, E., Lin, F.-C. & Koper, K.D., 2017. Determination of Rayleigh wave ellipticity across the Earthscope Transportable Array using single-station and array-based processing of ambient seismic noise, *Geophys. J. Int.*, **208**(1), 234–245.
- Xiao, H., Xue, M., Pan, M. & Gao, J., 2018. Characteristics of microseisms in south china, *Bull. seism. Soc. Am.*, **108**, 2713–2723.
- ZAMG – Central Institute for Meteorology and Geodynamics, 2006, Province Südtirol.
- ZAMG – Zentralanstalt Für Meteorologie Und Geodynamik, 1987. *Austrian Seismic Network*, International Federation of Digital Seismograph Networks, doi:10.7914/SN/OE.
- Zhao, L. *et al.*, 2015. First seismic evidence for continental subduction beneath the Western Alps, *Geology*, **43**(9), 815–818.
- Zhao, L., Paul, A. & Solarino, S., RESIF, 2016. *CIFALPS temporary experiment (China-Italy-France Alpes seismic transect)*, RESIF – Réseau Sismologique et géodésique Français, doi:10.15778/RESIF.YP2012.

## SUPPORTING INFORMATION

Supplementary data are available at *GJI* online.

**Figure S1.** Amplitude spectrum for four representative seismic stations. (a) Location of station FUSIO in Switzerland (network CH, Switzerland seismic network, Swiss Seismological Service (SED) At ETH Zurich 1983). (b) Locations of three stations in Greece:

KPRO (network HT, Aristotle University Of Thessaloniki Seismological Network, 1981); KZN (network HL, National Observatory of Athens Seismic Network, National Observatory of Athens, I.O.G. 1999); THL (network MN, MedNet Project Partner Institutions 1990). (c)–(f) Average spectrum of the four representative seismic stations in 2018. The black and blue arrows respectively indicate the Primary and Secondary microseismic peaks defined by the local maximum in period range 10–20 and 2.5–10 s. The orange arrow indicates a subtle local maximum observed for stations in Greece as discussed in Section 2 (Data and Data Processing).

**Figure S2.** Spatial distribution of the mean energy ( $E$ ) over the (a1)–(a3) years, (b1)–(b3) summer and (c1)–(c3) winter seasons in three period bands PB1 2.5–5 s (left), PB2 5–10 s (centre) and PB3 10–20 s (right). We display the relative variation of this quantity to the spatial median as denoted at the top of each subplot. The black dashed lines in each subplot correspond to a simplified version of the geological boundaries shown in Fig. 1.

**Figure S3.** Measurements of the most energetic horizontal direction of wave propagation ( $\theta_E$ ) for stations in the part of the study area with the highest station density. The azimuth of each red segment refers to the mean direction at that station of  $\theta_E$  over the (a1)–(a3) year, (b1)–(b3) summer and (c1)–(c3) winter seasons in three period bands PB1 2.5–5 s (left), PB2 5–10 s (centre) and PB3 10–20 s (right). The rose diagram in the right-hand corner of each subplot displays the statistics of all stations. The black dashed lines in each subplot correspond to a simplified version of the geological boundaries shown in Fig. 1. The colour scale shows the direction of each line.

**Figure S4.** Uncertainties of the estimated energetic horizontal direction of wave propagation ( $\theta_E$ ) as shown in Fig. 5 and Fig. S3 in the Supporting Information.

**Figure S5.** Measurements of the dominant horizontal direction of Rayleigh wave propagation ( $\theta_R$ ) for stations in in the part of the

study area with the highest station density. The arrows show the direction towards which the waves propagate, while the colour code shows the direction from which the waves propagate, equivalent to back azimuth for earthquake data.  $\theta_R$  is shown over the (a1)–(a3) year, (b1)–(b3) summer and (c1)–(c3) winter seasons in three period bands PB1 2.5–5 s (left), PB2 5–10 s (centre) and PB3 10–20 s (right). The rose diagram in the right-hand corner of each subplot displays the statistics of direction (backazimuth, equivalent to the colour scale) of all stations. The black dashed lines in each subplot are simplified from the geological boundaries shown in Fig. 1 to emphasize geological structures discussed in the main text.

**Figure S6.** Uncertainties of the estimated dominant direction of Rayleigh wave propagation ( $\theta_R$ ) as shown in Fig. 6 and Fig. S5 in the Supporting Information.

**Figure S7.** Slowness versus distance plot of  $P$  and PKP waves computed using the  $\tau$ - $p$  traveltimes calculation functionality (Crotwell *et al.* 1999) of Obspy using the 1-D global Earth model IASP91 (Kennett & Engdahl 1991). The blue arrows on the right side of the plot indicate incidence angles of corresponding slowness.

**Figure S8.** Same as Fig. 11, with information added about major Earthquakes. Comparison between the  $A_H/A_V$  and Beampower Ratio in 2018 for network CH. The Beampower Ratio refers to the ratio between the cumulated beam power of surface waves (area with velocity in the range 2.5–5 km s<sup>-1</sup>) and the cumulated beam power of surface and teleseismic body waves (summing the beampower of the area with velocity >20 km/s and the area corresponding to the range 2.5–5 km s<sup>-1</sup>). The days with earthquakes of magnitude bigger than 6.5 are shown with yellow lines and bigger than 7 with blue lines.

Please note: Oxford University Press are not responsible for the content or functionality of any supporting materials supplied by the authors. Any queries (other than missing material) should be directed to the corresponding author for the paper.